

Rowan University

Rowan Digital Works

Faculty Scholarship for the College of Science & Mathematics

College of Science & Mathematics

10-2022

Multifunctional silk fibroin – Poly(L-lactic acid) porous nanofibers: Designing adjustable nanopores to control composite properties and biological responses

Hangling Gu

Fang Wang

Hao Liu

Kyle Printon

Xiao Hu

Rowan University, hu@rowan.edu

Follow this and additional works at: https://rdw.rowan.edu/csm_facpub

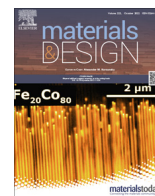


Part of the [Physics Commons](#)

Recommended Citation

Gu, Hangling; Wang, Fang; Liu, Hao; Printon, Kyle; & Hu, Xiao. Multifunctional silk fibroin – Poly(L-lactic acid) porous nanofibers: Designing adjustable nanopores to control composite properties and biological responses. *Materials & Design*, October 2022, 111053.

This Article is brought to you for free and open access by the College of Science & Mathematics at Rowan Digital Works. It has been accepted for inclusion in Faculty Scholarship for the College of Science & Mathematics by an authorized administrator of Rowan Digital Works.



Multifunctional silk fibroin – Poly(L-lactic acid) porous nanofibers: Designing adjustable nanopores to control composite properties and biological responses



Hanling Gu ^{a,b}, Fang Wang ^{a,b,*}, Hao Liu ^{a,b}, Kyle Printon ^{c,d}, Xiao Hu ^{c,d,e,*}

^a Center of Analysis and Testing, Nanjing Normal University, Nanjing 210023, PR China

^b School of Chemistry and Materials Science, Nanjing Normal University Jiangsu, Nanjing 210023, PR China

^c Department of Physics and Astronomy, Rowan University, Glassboro, NJ 08028, USA

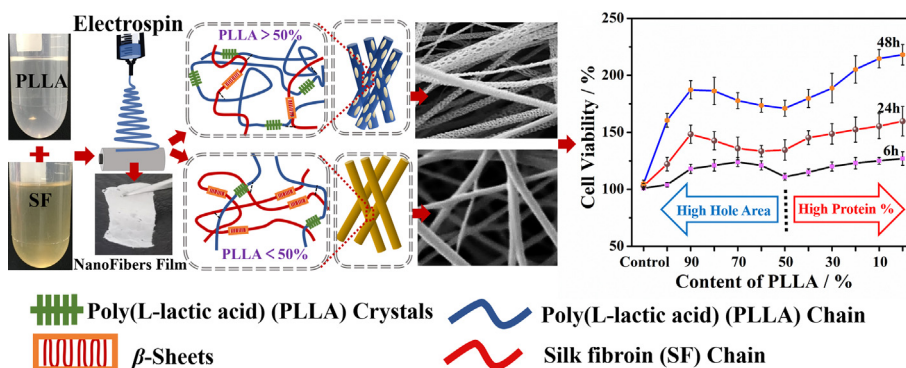
^d Department of Biomedical Engineering, Rowan University, Glassboro, NJ 08028, USA

^e Department of Molecular and Cellular Biosciences, Rowan University, Glassboro, NJ 08028, USA

HIGHLIGHTS

- First design of tunable nanopore structures on single fibers of electrospun silk-poly(lactic acid) blends via varying protein concentrations.
- Adjustable structure and hydrophilicity, excellent thermal stability and controllable biodegradation.
- Porous fibers promote cell attachment and manipulate cell proliferation.
- Lyotropic and thermally induced phase separation were responsible for the pore-forming on nanofibers.

GRAPHICAL ABSTRACT



ARTICLE INFO

Article history:

Received 21 March 2022

Revised 5 August 2022

Accepted 8 August 2022

Available online 10 August 2022

Keywords:

Poly(lactic acid)

Silk fibroin

Electrospinning

Porous fibers

Tissue engineering

ABSTRACT

Nano-scale renewable porous materials have a wide range of applications in the biomedical field such as tissue engineering and biosensors due to their high biocompatibility and large surface area. In this study, a composite of silk fibroin and poly(L-lactic acid) was electrospun together to form a porous nanofiber biomaterial with 11 blending ratios to tune the porosity of the single fibers (19.3–49%). This is highly advantageous as porous fibers effectively promoted cell attachment and proliferation while also manipulating cell growth. The protein-polymer molecular interactions, structures and crystal contents, as well as the melting and glass transition behaviors of the composites were determined. Results reveal that varying silk fibroin content can directly tune the nanopore structure of each individual fiber. The composite nanofibers have a much higher thermal stability when compared to the pure silk or PLA nanofibers. Besides, as the SF concentration increased from 0% to 100%, the hydrophilicity of the electrospun composite fibers increased (contact angle decreased from 135° to 103°), and the enzymatic degradation residues also increased from 20% to 95%. This study provides a unique method for tuning nano-fabrication properties of electrospun protein-polymer fibers that can be widely useful in the fields of biomedicine and sustainable materials.

© 2022 The Authors. Published by Elsevier Ltd. This is an open access article under the CC BY-NC-ND license (<http://creativecommons.org/licenses/by-nc-nd/4.0/>).

* Corresponding authors at: Center of Analysis and Testing, Nanjing Normal University, Nanjing 210023, PR China (F. Wang). Department of Physics and Astronomy, Rowan University, Glassboro, NJ 08028, USA (X. Hu).

E-mail addresses: wangfang@njnu.edu.cn (F. Wang), hu@rowan.edu (X. Hu).

1. Introduction

Porous materials are commonly used in drug delivery [1,2], tissue regeneration [3,4], filtration materials [5] and substrates for the encapsulation [6] due to their large surface area, large pore volume and adjustable pore size that can be tuned to optimized cell growth and repair. Current methods for preparing porous nanomaterials mainly include solvent casting [7], salt leaching [8], dry spinning [9], wet spinning [10], 3D printing [11] and electrospinning [12]. However, it is much more difficult to make nanopores on one-dimensional materials such as nanofibers. Dry spinning is not an ideal porous scaffold fabrication method, because it requires high solvent viscosity and volatility and it is difficult to achieve continuous spinning [13]. Although wet spinning is simple and easily repeatable, the mechanical properties of its fiber are not ideal [14,15]. 3D printing is also not an efficient fabrication method for nanopores as the cost is relatively high, with relatively low manufacturing efficiency and insufficient precision [16,17]. Electrospinning has attracted many attentions due to its easy operation, low cost and wide adaptability in the preparation of 1-D nano or ultrafine fibers with different nanopore structures [18,19].

The advanced development of composite materials has suggested that we can selectively process a variety of natural and synthetic polymers into nanomaterials to overcome the poor performance of single-phase materials, and improve the mechanical, thermal, rheological and biodegradability properties of polymers for regenerative tissue engineering and drug delivery scaffolds [20,21]. In order to overcome the shortcomings of polylactic acid (PLA), such as low hydrophilicity and cell affinity [22,23], natural silk fibroin proteins can be added in varying concentrations to obtain a composite material with high biocompatibility and biodegradability [24,25]. Regenerated silk fibroin (SF) is a natural fibrous protein derived from silkworm cocoon fibers, with good mechanical strength and flexibility due to the formation of β -sheet crystalline structures between molecular chains [24,25]. Poly-lactide (PLA) is a green synthetic polymer with good biocompatibility and degradability, which is an environmentally friendly material obtained from natural corns and cereals [22,23]. The composite materials of SF proteins and PLA polymers have demonstrated superior physical and biological properties compared to their individual components. Gao et al. [26] found that the multi-layer mineralized polylactic acid/silk fibroin structures enhanced cell growth and differentiation. Yan et al. [27] used phenylenediamine to promote the formation of pores on the surface of several silk fibroin/polylactic acid fiber scaffolds, with mechanical properties and biocompatibility favorable for a cardiac scaffold, a similar result was also reported by Kyu et al. [28]. However, the fabrication of surface pores on existing composite nanofibers is quite cumbersome and the material itself is also eroded by harmful solvents [29].

Therefore, many researches focused on the topic of various fibers fabrications and properties for polylactic acid and silk fibroin [25,30,31]. However, among these studies, the proportion of silk fibroin does not exceed 50%, and only smooth fibrous membranes were formed. Specifically, the regulation of nanopores on each fiber of PLLA/silk fibroin composites fiber film, and the pore-forming mechanism of nanofibers by the addition of silk fibroin at full proportion mixture ratios have not been reported yet. Such type of composite fibers is very advantageous in many potential applications of drug delivery, facial mask accessories and scaffolds for rapid cell growth, etc.

In this study, a unique solvent system was used to compound polylactic acid and silk fibroin in full proportions (10:0, 9:1, 8:2, 7:3, 6:4, 5:5, 4:6, 3:7, 2:8, 1:9 and 0:10) and create a tunable fibrous mat with nanopores. The resulting composite materials was analyzed using scanning electron microscopy (SEM), Fourier

transform infrared spectroscopy (FTIR), differential scanning calorimetry (DSC), thermogravimetric analysis (TGA), X-ray diffraction systematically analyses (XRD), X-ray photoelectron spectroscopy (XPS), water contact angle measurement, biological enzyme degradation and cytotoxicity tests, which determined the microstructure, stability and biological performance of the composite fiber material. This study provides a basis for further study on the application of novel porous nanofiber materials in tissue repair and regeneration, drug coating and delivery among other applications.

2. Materials and experiments

2.1. Materials

Materials and reagents were obtained from the following sources: Chinese silk fibroin (SF) (extracted from *Bombyx mori* silkworm cocoons, Dandong July Trading Co., Ltd., China), Poly(L-lactic acid) (PLLA, Shenzhen Yisheng New Material Co., Ltd., China), NaHCO_3 (AR purity, Shanghai Lingfeng Chemical Reagent Co., Ltd., China), CaCl_2 (96.00%, AR purity, Xilong Science Co., Ltd., China), Formic acid (88.00%, AR purity, Xilong Science Co., Ltd., China), Methylene chloride (98.00%, AR purity, Xilong Science Co., Ltd., China); Proteinase K ($\geq 95.00\%$, Phygene Biotechnology Co., Ltd., China).

2.2. Preparation of PLLA/SF nanofiber mats

Calcium chloride powders were first weighed and mixed with formic acid to prepare a 4 wt% calcium chloride-formic acid (FA) solution as the solvent. Silk fibroins were then dissolved into the FA solution, and finally prepared into 8 wt% silk fibroin solution. Then PLLA powders were dissolved in dichloromethane to prepare a PLLA solution with a concentration of 8 wt%. The above-mentioned PLLA solution was poured into silk fibroin solution and mixed at various ratios (10:0, 9:1, 8:2, 7:3, 6:4, 5:5, 4:6, 3:7, 2:8, 1:9 and 0:10), respectively. And each mixture was stirred for half an hour at ambient temperature. Then sonicated for 30 min for thorough mixing to obtain final electrospinning solution. The sample name was respectively marked as PS100 (pure PLLA), PS90, PS80, PS70, PS60, PS50, PS40, PS30, PS20, PS10 and PS0 (pure silk). The syringe containing the electrospinning solution was placed in a single-channel syringe pump. The flow rate was set to 0.2 mL/h, and the voltage was set to 15 kV. The distance between the syringe needle and the receiving device was 10 cm, and the fibers were spun over a period of 5 h.

2.3. Morphology analysis

The samples were first placed in a sputtering apparatus for gold plating with the current set to 20 mA. Each surface of the samples was gold plated for 30 s four times. The SEM (JSM-7600F, JEOL, Japan) working voltage was 10 kV and the working distance was 15 cm. The total porosity and single fiber porosity was calculated through various area (A_1 and A_2) obtained by Image J software. For total porosity calculation (Equation (1)) [32], A_1 and A_2 is the area of all holes and the total fiber area in specific region of the image (nm^2), respectively. For porosity on single fiber (Eq. (1)), A_1 and A_2 is the area of all holes on a single fiber and the single fiber total area in the image (nm^2), respectively. The fiber diameter and pore size on single fiber were also obtained via Image J software. At least three replicate samples were analyzed for each material [32]:

$$\text{Porosity}(\%) = \frac{A_1}{A_2} \times 100\% \quad (1)$$

2.4. Structural analysis

2.4.1. Fourier transform infrared spectrometer (FTIR)

FTIR analysis was performed using a Bruker FTIR Spectrometer (Vertex 70, Bruker, Germany) with a deuterated triglycine sulfate detector and a multiple-reflection, horizontal MIRacle ATR attachment (using a Ge crystal) with clamping mode. Each sample (untreated and treated with 30 mins methanol) was placed on the Ge crystal to collect the sample signal with a resolution of 4 cm^{-1} . The number of scans selected was 64 times, and the infrared spectrum was measured in the wave number range of $4000\text{--}400\text{ cm}^{-1}$. Fourier self-deconvolution (FSD) of the IR spectra covering the amide I region was performed by Opus 5.0 software. Deconvolution was performed using Lorentzian line shape with a half-bandwidth of 25 cm^{-1} and Gaussian functions, as well as a noise reduction factor of 0.3. FSD spectra were then curve-fitted to measure the relative areas in the amide I region. The fitted individual peaks can be assigned as side chains (S), β -sheets (B), random coils (R), α -helix (A) and turns (T) according to the literature method [33,34].

Additional FTIR analysis was performed using a FTIR Spectrometer (Vertex 70, Bruker, Germany) in contactless reflectance sampling module (over an aluminum foil reflective surface). Measurement spot distance is 4 mm. Background spectra was collected directly on the aluminum foil surface. The FTIR settings were as follows: 64 scans for each acquisition, spectral resolution of 4 cm^{-1} , open windows, and spectral range of $4000\text{--}600\text{ cm}^{-1}$.

2.4.2. X-ray photoelectron spectrometer (XPS)

The XPS analysis was carried out using an EscaLab Xi + instrument (Thermo Fisher, UK) equipped with monochromatic Al-K α radiation ($h\nu = 1486.6\text{ eV}$). X-ray was performed at a working voltage of 40 kV at $2^\circ/\text{min}$. C1s at 284.5 eV was considered the reference for all Binding Energies (BE). The spectra of C 1s was analyzed using the OriginPro2021b software.

2.4.3. ^{13}C Solid-state Nuclear Magnetic Resonance (SS-NMR)

Spectra was performed on a SS-NMR (Bruker, AVANCE III 400WB, Germany) spectrometer at 9.4 T with a frequency of 100.62 MHz. Samples were packed into the 4-mm zirconia rotors. For each ^{13}C CP-MAS test, the contact time was 2 ms, the recycle delay was 2–4 s, which were adjusted to three times of 1H for T1 values. A technology of ramp-contact and a program of spinal 64 decoupling pulse were used. The number of scans for ^{13}C CP-MAS measurements was 2000–10000 with a rotor spinning rate of 14 kHz. The spectra was also calibrated using the methine carbon atoms of adamantane as an external standard ($d = 29.47\text{ ppm}$).

2.4.4. X-ray diffraction (XRD)

XRD Analyses were performed by using a D/max 2500VL/PC diffractometer (Rigaku Corporation, Japan). Cu-K α radiation was generated by the source with a graphite diffracted beam monochromator operated at 40 kV and 100 mA. Here, $K = \cos^2 2\theta_M$, where $2\theta_M$ is the diffraction angle of monochromator. $\alpha\text{-SiO}_2$ was used as a standard to measure the width of samples in the experiment. Diffraction data were acquired with an increase of 2θ from 5° to 50° at a $5^\circ/\text{min}$ scanning rate.

2.5. Thermal analysis

2.5.1. Differential scanning calorimeter (DSC)

Thermal properties of PLLA/SF samples were analyzed by differential scanning calorimetry (DSC) on a DSC7000X instrument (Hitachi, Japan) in nitrogen atmosphere. About 5 mg of sample was massed and sealed in an aluminum pan with an empty aluminum pan as the reference. Under the standard DSC mode, the

nitrogen flow rate was set to 30 mL/min and the heating rate was $10\text{ }^\circ\text{C}/\text{min}$. The temperature modulated DSC (TMDSC) mode was used with the following settings: $5\text{ }^\circ\text{C}/\text{min}$ heating rate, a frequency of 0.02 Hz, a temperature amplitude of $3\text{ }^\circ\text{C}$ and a temperature range of -20 to $200\text{ }^\circ\text{C}$. Each sample was tested at least 3 times. The heat flow and temperature of the instrument have been calibrated with the standard indium, and the specific heat was determined from the sapphire calibration scans. The glass transition temperature (T_g), melting temperature (T_m) and melting enthalpy (ΔH_m) were calculated by the NEXTA Job Gallery software of Hitachi. The crystallinity (X_c) was estimated using the following Eq. (2) [35],

$$X_m(\%) = \frac{\Delta H_m}{\Delta H_0} \times 100\% \quad (2)$$

where ΔH_m (J/g) is the heat of melting of the samples, and ΔH_0 is 93.6 J/g which is the melting enthalpy of 100% crystalline PLLA reported in literature [35].

2.5.2. Thermogravimetric analysis (TGA)

The thermal stability of the samples was investigated by thermogravimetric analysis (Pyris 1, PerkinElmer, USA). The temperature of thermogravimetric analyzer was used to calibrated through Alumel and Nickel standard sample. 100 mg standard mass has been used to calibrate the measured weight of TG. The nitrogen flow rate was set at 50 mL/min, 5–6 mg of sample was heated from room temperature to $600\text{ }^\circ\text{C}$ at a heating rate of $10\text{ }^\circ\text{C}/\text{min}$. The first derivative of the thermogravimetric analysis curve (DTG) obtained from Pyris series software (PerkinElmer, USA) was also presented to reflect the degradation rate and the intermediate degradation temperatures. Each sample was tested at least 3 times.

2.6. In vitro biodegradation

Proteinase K was dissolved in a 0.1 M (pH = 8.6) Tris-HCl buffer solution to obtain a concentration of 0.2 mg/mL proteinase K solution. The prepared composite nanofiber mat was placed in a centrifuge tube and 5 mL of proteinase K solution was added. The centrifuge tubes were then stored in a $37\text{ }^\circ\text{C}$ water bath for the time periods up to 6 days (6 d). After 1, 2, 4 and 6 days the proteinase K solution was individually removed, then the samples were taken out and washed thoroughly with distilled water and dried by vacuum-dried oven at $37\text{ }^\circ\text{C}$ temperature until the weights remained constancy. Finally, the remaining mass was weighed, respectively. Throughout the entire process, fresh protease K solution was replaced every 24 h to ensure that the enzyme activity was maintained at the ideal level. The samples without enzyme in aqueous solution were also evaluated as the control data. Simultaneously, other two sets of same experiments were set up for all the above samples. The degradation of samples treated with methanol for 30 min were also measured using the same experimental method mentioned above.

2.7. Hydrophilic analysis

A contact-angle measuring instrument (DSA30S, KRÜSS, Germany) was used to test the change in the hydrophilicity of the material. The lying drop method was utilized, and a continuous tracking measurement mode was used to save the image every second. The contact angle of the liquid was measured and was repeated at least three times to determine the average value.

2.8. Biocompatibility analysis

Biological response: Mouse fibroblasts (L929) were cultured with a modified DMEM medium that consisted of 10% FBS and were placed in a humidified incubator at 37 °C and 5 % CO₂. Trypsin was used to detach viable cells from the culture surface for further study. An MTT Assay was conducted to determine the toxicity of the nanofibers. All nanofiber samples were sterilized before seeding to prevent contamination. 100 μL of L929 cell suspension was seeded in a 96-well plate at a cell density of 1 × 10⁴ cells/mL. After 6, 24, and 48 h the medium was removed from each well, respectively. The fibers and cells were rinse twice with PBS. Finally, 200 μL of MTT solution (0.5 mg/ml) was added to each well plate to conduct the MTT Assay. After 4 h, the methyl sulfoxide solution was replaced, and the cultures were shaken for 10 min. The absorbance of each well was measured at 570 nm through microplate reader (EL-X800, BioTek, USA). This process was repeated 3 times for each sample, and the cell viability was calculated by Eq. (3) [36]:

$$\text{Viability} = \frac{D_s}{D_c} \times 100\% \quad (3)$$

where D_s is the absorbance of the cell culture solution exposed to the films, D_c is the absorbance of the control solution.

In order to determine cell morphology, the cells were cultured on the nanofiber mats for 6, 24, and 48 h and were washed with PBS. Then it was fixed in 4% paraformaldehyde solution for 15 min. Finally, DAPI (4',6-Diamino-2-phenylindole) fluorescence staining was used to stain the nucleus for 30 min. Cells were also imaged under a fluorescent microscope using a camera (Nikon 80I, Japan) [37]. All biological experiments were performed at least three times.

2.9. Statistical analysis

All experimental data were expressed as mean ± standard deviation (SD). Statistical analyses were performed using one-way ANOVA analysis ("analysis of variance"). Differences between values was considered statistically significant with P or p values.

3. Results and discussion

3.1. Morphology analysis

Fig. 1 shows the schematic preparation of silk/poly(lactic acid) composite nanofibers based on electrospinning method (Fig. 1a). A morphological image of PLLA/SF = 80/20 (PS80) nanofibers with nanopores is shown in Fig. 1b, and the nanofiber diameter and porosity of all composites with different mixing ratios were calculated using the Image J software (Fig. 1c, 1d). SEM images of all samples, histograms of fiber diameter distribution (grey, black curves) and pore size distribution on single fibers (blue, red curves) are shown in Figure S1. Most pure PLLA fibers appeared spindle-shaped, with uneven diameters and contained a large number of beaded structures with large gaps between each fiber (Figure S1a and S1a, PS100) [38,39]. The fiber diameter of pure PLLA was mainly distributed between 0.5 and 2.2 μm, and the average diameter was 996 ± 72 nm (Fig. 1c). The pure PLLA fibers contained smaller pore sizes (44 ± 11 nm) because of the low boiling point of the solvent, the hydrophobicity of PLLA as well as their low viscosity and conductivity [39]. When silk was added, even in small ratios, the morphology was greatly affected. For example, the average fiber diameter of sample PS90 reduced to 694 ± 85 nm, while the average pore size increased to 70 ± 15 nm (Figure S1b). As the SF ratio was increased, the fibers diameter and pore size grad-

ually became more uniform and the fibers showed reduced beading structures. For PS80, the fibers diameter is 610 ± 90 nm (Fig. 1c), and pore size is 58 ± 10 nm (Figure S1c). The total porosity and the porosity on each fiber gradually decreased with the increasing of the silk fibroin ratio, and both have the maximum value 54.7 ± 3.1 % and 49.0 ± 3.0 % for sample PS90 (Fig. 1d), respectively. However, for samples with SF ratios higher than 60%, there are no clear pores on individual fibers and the total porosity does not change significantly. Samples PS60 showed the largest average fiber diameter (1022 ± 118 nm) while also displayed globules at the intersection of each fiber (Figure S1e, PS60). This was different when compared to the PS80 sample as these fibers were distinctly individual and did not adhere to each other. Previous studies [39–41] have shown that this phenomenon is most likely caused by the electric field that forces the electrospun fibers to adhere to each other if the solution has a high viscosity. This results in less uniform fibers that stick together. This is also evident as SF to increase as the viscosity of the solution decreases, and the fiber gradually becomes more uniform and swelling on the fiber surface occurs (Figure S1g ~ S1j, PS40 ~ PS10). This is also because the polar amino acids in silk fibroin can increase the electrical conductivity of the blend and promote stretching of the electrospun fiber [42–44]. However, unlike composite samples, pure silk fibroin (Figure S1k, PS0) showed uneven fiber thickness, which is consistent with the findings of Shao et al. [43].

3.2. Structural analysis

FTIR is a powerful tool for protein conformation analysis, and widely used in the study of protein-polymer composites [44], such as determination the specific infrared absorption peaks of each component for silk fibroins and PLLA. Fig. 2a shows the normalized absorbance infrared of nanofibers consisting of different PS samples in the wavenumber region of 1000–2000 cm⁻¹.

Generally, for the silk protein, the FTIR spectral region within 1700–1600 cm⁻¹ is attributed to the peptide backbone of Amide I absorptions and 1600–1500 cm⁻¹ to the Amide II [33]. For the pure silk nanofiber in our work (Fig. 2a, PS0), the peaks at 1646 cm⁻¹, 1545 cm⁻¹ and 1247 cm⁻¹ were observed which is correlated to the random coils structure [33,45,46].

For PLLA, the significant IR absorption bands at 1753 cm⁻¹, 1452 cm⁻¹, 1182 cm⁻¹ and 1086 cm⁻¹ are associated with C = O stretching of carbonyl group, C-H deformation vibration, C-O-C stretching and C-O antisymmetric stretching, respectively [47,48,49], as shown in Fig. 2a (PS100). By comparing the FTIR spectra of SF/PLLA composites, it was exhibited that with the increase of SF content, the intensity of spectra at 1753 cm⁻¹, 1182 cm⁻¹ and 1128 cm⁻¹ as well as 1086 cm⁻¹ gradually decreased, while the intensity at 1646 cm⁻¹ and 1545 cm⁻¹ gradually increased. Besides, 1753 cm⁻¹ for PLLA is moved to 1757 cm⁻¹, and 1268 cm⁻¹ attributed to PLLA is gradually shifted to 1247 cm⁻¹ of SF. These results implies that there are interactions between SF and PLLA chains [25].

Furthermore, peak fitting was performed on the range of 1720–1580 cm⁻¹ in the amide I region (Fig. 2b) through a deconvolution method, to understand the structural changes of PLLA and SF with different composite ratios. The fitted individual peaks can be assigned as side chains (S), β-sheets (B), random coils (R), α-helix (A) and β-turns (T) [33,34]. Table 1 shows that PS0 was mainly composed of random coils and α-helices (46.8%), and the content of β-sheets is about 24.2% which is similar to the literature [50]. With the increase of the PLLA content in the PS composite nanofiber film, the β-sheet content in silk fibroin decreased from 24.2% to 16.8%, while the content of random coils and α-helices increased from 46.8% to 51.9%, and the turns content increased from 24.8%

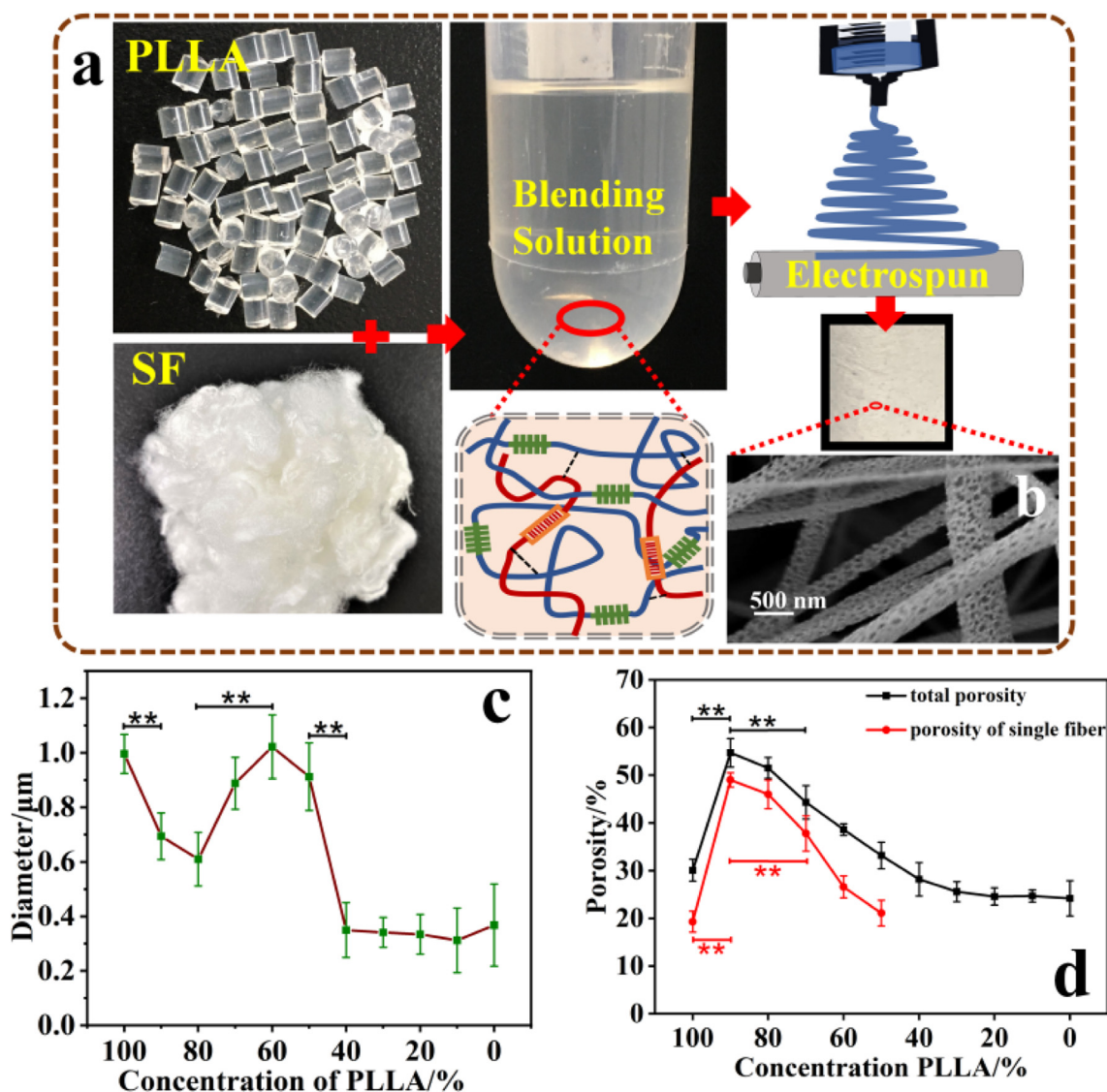


Fig. 1. (a) Schematic preparation of silk/polylactic acid composite nanofibers based on electrospinning method; (b) SEM image of porous PS nanofibers with a mass ratio of PLLA/SF = 80/20 (PS80); (c) average fiber diameter, and (d) the total porosity and the porosity of single fiber for different PS composites plotted as the function of PLLA concentration, respectively (** $p < 0.005$, $N \geq 50$).

to 29.1%. When the samples were treated with methanol, the content of β -sheets in all composites increased significantly. Studies have shown [51–53] that the β -sheets structure in silk fibroin can promote the formation of protein stability and insolubility. Although analysis of the structure of silk fibroin using ATR-FTIR is a standard method [33,34,46,49], some studies reported [54] that the ATR tip pressure might induce structural change of the protein. Therefore, we added another set of experiments for the samples (PS0-PS50, silk protein dominated) using FTIR scans with a contactless reflectance module, and compared with the results to the ATR module (Figure S2). Both characteristic peaks of silk fibroin and poly(lactic acid) appeared in the composites samples, and all structural contents were relatively close to those detected by the ATR module (Table S1), indicating that the ATR tip pressure had less effect on the sample structure.

XPS is used to accurately measure the inner electron binding energy of atoms and their chemical shifts [55–57]. Pure PLLA (PS100) mainly contains C, H, and O elements (Fig. 2c). The addition of silk fibroin (PS90, PS80, PS70, PS60, PS50, PS40, PS30, PS20 and PS10) created composite materials that show increased

peaks for C, N, and O elements. Following the literature [58–61], the PS composites was subjected to the peak fitting of C element (Fig. 2d), and results were listed in Table 2. Specifically, for SF, the vicinity of 284.7 eV and 286.7 eV in C1s are respectively attributed to C–C, C–O or C–N groups (referred to as C–C_s, C–O_{ps} and C–N_s) [62]. For PLLA, 285.2 eV, 286.7 eV, 288.7 eV and 291.0 eV were attributed to C–H, C–O, C=O and O–C=O groups, respectively (referred to as C–H_p, C–O_{ps}, C=O_p and O–C=O_p) [63]. Chen et al [64] demonstrated that the intensity of the C1s peak at 285.9 eV in the SF/polydopamine hydrogel was significantly increased compared to the pure SF hydrogel. In our study, as the content of silk fibroin increases, the content of C–C_s and CO/CN increased while the content of C–H_p and C=O_p decreased. However, the O–C=O_p content first decreased (PS100-PS40) and then increased (PS40-PS20), implying a potential hydrogen interaction between the C=O group of the poly(lactic acid) and the O–H bonds on the silk fibroin.

Solid State Nuclear Magnetic Resonance (SS-NMR) was then used for further structural analysis of the protein-polymer composites [65], since the isotropic chemical shift of carbon atoms in the protein chains is closely related to its molecular structure

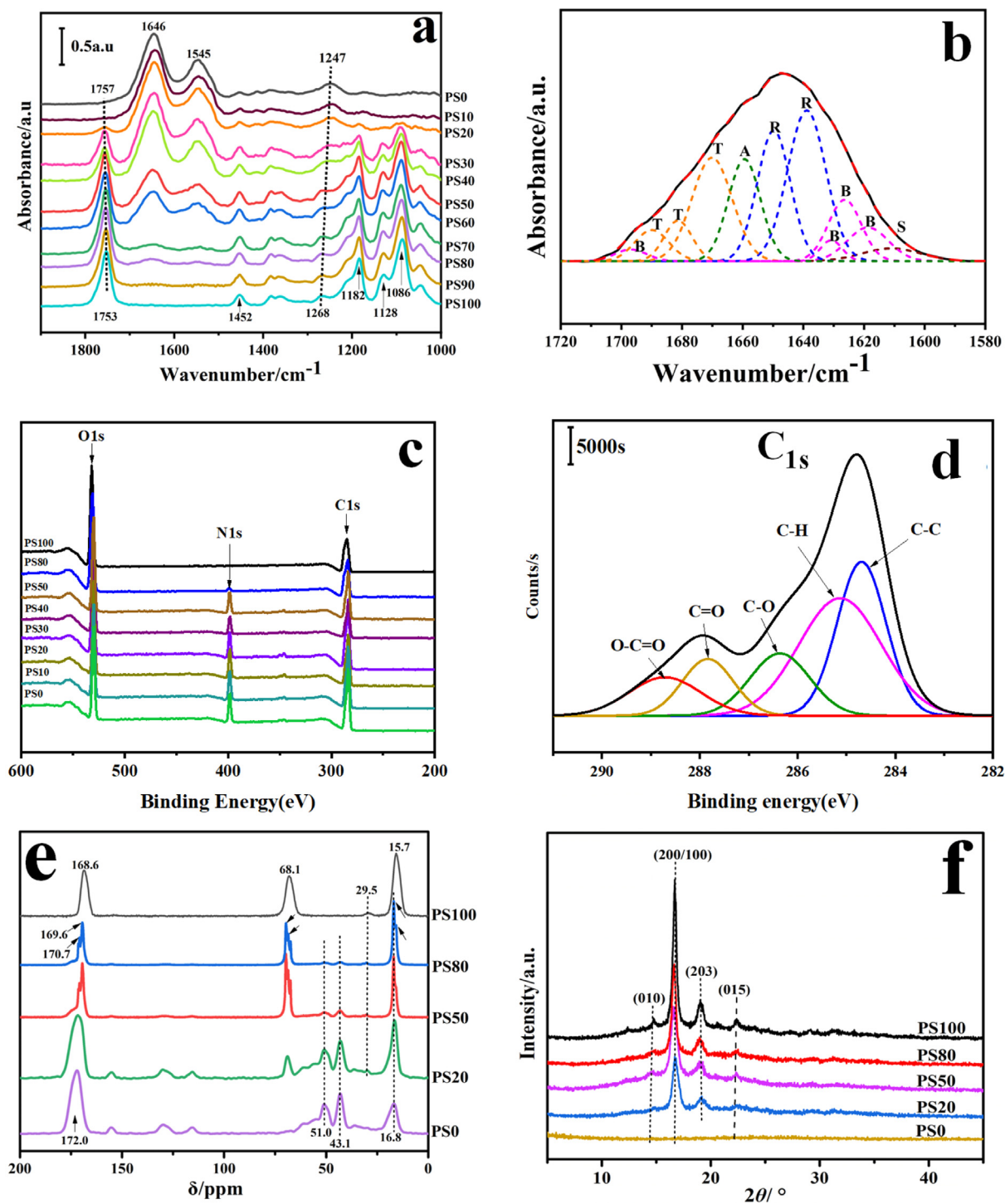


Fig. 2. (a) Infrared spectra (ATR mode) of PS composite nanofiber films with different mass ratios in 1900–1000 cm^{-1} , and (b) an curve fitting example of PS20 composite fiber spectra in the amide I region (1720–1580 cm^{-1}); the black line represents the best fit curve, the colored short dash lines represent the contributions to the amide I region and are marked as random coil (R), β -sheets (B), α -helices (A), turns (T), and side chains (S); (c) High resolution X-ray photoelectron spectroscopy (XPS) spectra of C, N, O, Ca in the PS nanofibers, ranging from 600 to 200 eV, and (d) a peak fitting example of PS20 nanofiber XPS spectrum in C_{1s} region; (e) ^{13}C Solid State Nuclear Magnetic Resonance spectra, and (f) X-ray diffraction spectra of the PS100, PS80, PS50, PS20 and PS0 composite nanofibers.

(Fig. 2e). For pure PLLA sample (PS100), the peak at 168.6 ppm was attributed to carbonyl carbon ($\text{C}=\text{O}$), the peak at 15.7 and 68.1 ppm were associated with methyl methane, and the peak at 29.5 ppm was assigned to methylene C_1 [65–67]. For the pure SF sample (PS0), major amino acid residues conformation was correlated to the ^{13}C chemical shifts [67], such as 43.1 ppm and 51 ppm for alanine $\text{C}\alpha$, 172.0 ppm for $\text{C}=\text{O}$ [68]. For composite fibers

(PS80, PS50, and PS20), the peak intensity and peak position shift slightly with the change of SF content. For example, for the PS80 sample, the peak at 168.6 ppm moved to 169.6 ppm, and emerged with the shoulder peak at 170.8 ppm. A similar study was reported by Wu et al. [69] that the peak at $\delta = 175.05$ ppm split into two bands (177.06 and 178.26 ppm) in the composites of acrylic acid grafted polylactide and corn starch, which attributed to the inter-

Table 1
Infrared curve (ATR mode) fitting results of PLLA, SF and their composite nanofiber materials.

Sample	Silk/%	β -sheet	α -helix and random coils/%	Turns/%	Side chains/%	Silk amorphous in sample/% ^b
PS0	100	24.2/49.6 ^a	46.8/24.5 ^a	24.8/23.4 ^a	4.2/2.5 ^a	50.4
PS10	90	23.7/47.8 ^a	48.0/25.4 ^a	25.0/24.0 ^a	3.3/2.8 ^a	47.0
PS20	80	22.8/45.8 ^a	48.8/26.7 ^a	25.3/24.3 ^a	3.1/2.5 ^a	43.4
PS30	70	21.7/42.0 ^a	48.9/28.5 ^a	26.1/25.2 ^a	3.3/4.3 ^a	40.6
PS40	60	21.0/40.7 ^a	49.5/29.1 ^a	26.7/26.7 ^a	2.8/3.5 ^a	35.6
PS50	50	20.1/38.5 ^a	50.2/31.8 ^a	27.3/27.2 ^a	2.4/2.5 ^a	30.8
PS60	40	19.6/37.1 ^a	50.4/32.5 ^a	27.5/28.1 ^a	2.5/2.3 ^a	25.2
PS70	30	18.9/35.5 ^a	50.8/32.9 ^a	28.0/28.7 ^a	2.3/2.9 ^a	19.4
PS80	20	18.1/34.5 ^a	51.2/33.8 ^a	28.4/29.1 ^a	2.3/2.6 ^a	13.1
PS90	10	16.8/33.1 ^a	51.9/34.5 ^a	29.1/29.7 ^a	2.2/2.7 ^a	6.7
PS100	0	/	/	/	/	0

^a β -sheet structure content after methanol treatment for 30 min. All calculated secondary structure fractions have the same unit (wt %) with a ± 2 wt% error bar.

^b Silk amorphous in sample/% = $(100 - X) \times w$, where, X represents β -sheet content after methanol treatment; w stands for the percentage content of silk fibroin in the composite fibers.

Table 2
The proportions of different groups in the C element peak of the PS composite.

Sample	C-C _s (%) ~284.8 eV	C-H _p (%) ~285.2 eV	C-O _{ps} /C-N _s (%) ~286.7 eV	C = O _p (%) ~288.7 eV	O-C = O _p (%) ~291.0 eV
PS100	–	30.2	23.4	21.3	25.1
PS80	8.7	26.1	27.9	12.4	24.9
PS50	15.4	21.8	28.8	15.6	18.4
PS40	21.0	18.7	27.1	15.0	18.2
PS30	23.3	17.5	26.0	13.8	19.4
PS20	25.6	13.6	28.3	8.9	23.6
PS0	63.3	–	36.7	–	–

*All calculated values have the same unit (wt%) with a $\pm 2\%$ error bar. s represents the chemical groups contained only in the silk molecules; p represents the groups contained only in the PLLA molecules; ps represents the groups contained in both PLLA and silk molecules.

action between the carboxyl group of acrylic acid and –OH group of corn starch. Zheng et al. [70] found that silk fibroin and hydroxybutyl chitosan molecules undergo hydrogen-bonding interactions when mixed, resulting in intensity changes and peak shifts in the NMR spectrum. These NMR results were consistent with previous results, showing strong interactions between silk and PLLA molecules.

In addition, the samples were also analyzed by XRD measurement (Fig. 2f). For pure PLLA, a strong diffraction peak near 16.7° (200/100) was attributed to the α crystal of PLLA [41,48,71]. The smaller 2 θ peaks at 18.7°, 22.3° and 14.8° correspond to the diffraction of (203), (015) and (010) crystal planes of PLLA, which were consistent with the literature [41,48,71]. The peak strength of PLLA decreased with the increase of SF content in the composite film. Simultaneously, by using a peak fitting software, XRD curves were deconvoluted to obtain the crystalline and amorphous structure contributions (Figure S3, Table S2). The pure PLLA sample had the highest mobile amorphous phase (X_{MAP}) content of all samples (~57%). With the SF content increasing, the content of crystalline phase (X_c) of PLLA in the composite films gradually decreased, and the contents of mobile amorphous phase (X_{MAP}) and rigid amorphous phase (X_{RAP}) gradually increased. This result showed that SF chains tended to inhibit the formation of PLLA crystals while promoted the formation of intermediate amorphous phases (such as X_{RAP}) between the SF and PLLA molecular domains to facilitate the interactions between the two components.

3.3. Thermal analysis and stability

DSC was used to obtain the thermophysical properties of polymer-protein blends. DSC is an important technology to obtain miscibility information of polymer blends by studying their glass transition temperature (T_g) and melting temperature (T_m) [72–74]. Studies have found [75–77] that the new T_g formed by blend-

ing two polymers can be between or exceed the glass transition temperatures of the two individual polymers. Fig. 3a shows the DSC heating curve obtained with varying ratios of PLLA/SF nanofiber composites. The PS fibers had a glass transition region, a cold crystallization region and a melting region. The exothermic cold crystallization peak appeared between 80 and 138 °C as the SF ratio increased, and the cold crystallization peak gradually shifted from 121 °C to 112 °C. The melting peaks was observed at the range of 138–168 °C. The size of the melting peak also decreased as the PLLA content decreased. Fig. 3b shows the reversing heat capacity curves of the PS composite nanofibers measured by TMDSC. The glass transition temperature of pure polylactic acid (PS100) was 55.6 °C while the melting temperature was 151.1 °C. The glass transition temperature of pure silk fibroin nanofibers (181.5 °C) was slightly higher than the SF films fabricated from the formic acid solution (162.5 °C) and the aqueous solution (176 °C) [34,78,79]. The co-existence of ordered domains of plain nanofibers caused the glass transition temperature of the amorphous phase to shift to a higher temperature [80]. As silk fibroin content increased, the glass transition temperature of the composite increased (Table 3), while the melting temperature decreased and gradually shifted into a single peak [81,82]. This also showed that the melting enthalpy value decreased while the specific heat capacity increment during T_g increased (Table 3). With the addition of silk fibroin, the crystallinity of PLLA calculated by DSC also decreased from 37.7 ± 2.5 (PS100) to 7.6 ± 1.0 (PS10), which was consistent with the result from XRD analysis (Table S2). These results suggested that the composite materials exhibited good miscibility that differed greatly from the pure fibers due to underlying molecular interactions of the two materials.

Thermogravimetric analysis (TGA) is used in this study to characterize the thermal stability and thermal decomposition mechanism of each composite material [83]. Fig. 3c and Figure S4a show the thermal degradation of PS nanofiber samples, while

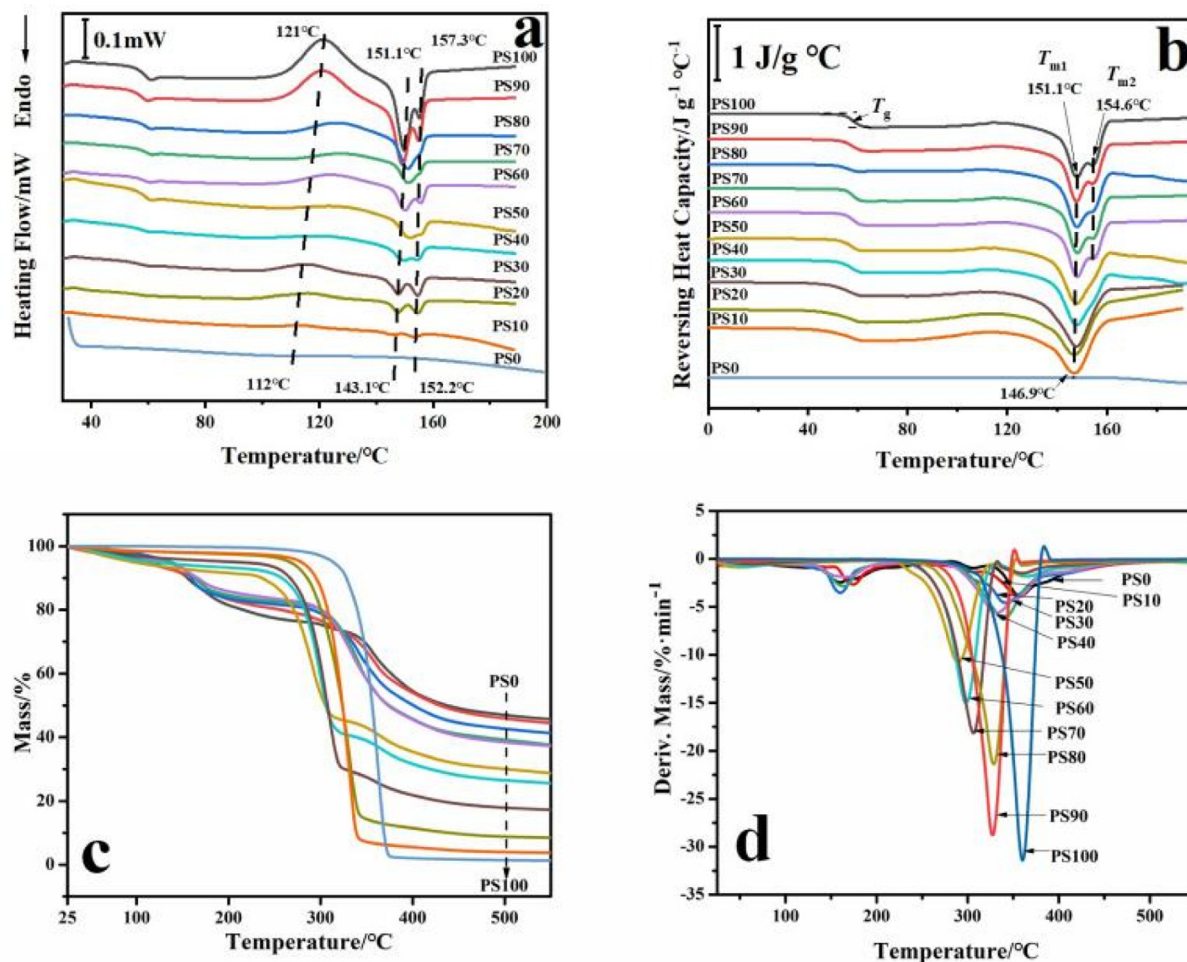


Fig. 3. (a) DSC heating curves of PS composite nanofiber mats with different ratios, and (b) reversing heat capacity curves of the PS nanofiber samples (modulation frequency is 0.02 Hz, modulation temperature amplitude is 3 °C, and heating rate is 5 °C/min); T_g , T_{m1} and T_{m2} represent the glass transition temperature, the first melting peak temperature and the second melting peak temperature, respectively. (c) TG curves of PS nanofibers heating from 25 to 550 °C at a rate of 10 °C/min, and (d) the first derivative of the mass percentage curves in (c).

Table 3

The glass transition temperature (T_g), melting temperature (T_{m1} and T_{m2}), melting enthalpy (ΔH_m) and heat capacity increment at T_g (ΔC_p) of PS nanofibers at different ratios.

Sample	SF/%	$T_g/^\circ\text{C}$	$T_{m1}/^\circ\text{C}$	$\Delta C_p/J\text{ g}^{-1}\text{ }^\circ\text{C}^{-1} (\times 10^{-2})$	$T_{m2}/^\circ\text{C}$	$\Delta H_m/J\text{ g}^{-1}$	$X_c/\%$
PS100	0	55.6 ± 0.7	151.1 ± 0.9	35.3 ± 0.4	154.6 ± 0.8	35.3 ± 0.1	37.7 ± 0.5
PS90	10	55.9 ± 0.5	150.9 ± 0.2	36.7 ± 0.3	154.5 ± 0.4	30.9 ± 0.3	33.0 ± 0.8
PS80	20	56.4 ± 0.6	150.7 ± 0.4	37.5 ± 0.5	154.0 ± 0.3	28.4 ± 0.2	30.3 ± 0.3
PS70	30	57.2 ± 0.9	149.9 ± 0.6	37.6 ± 0.3	153.6 ± 0.6	26.2 ± 0.4	28.0 ± 0.9
PS60	40	58.5 ± 0.7	149.7 ± 0.8	38.2 ± 0.5	/	23.6 ± 0.5	25.2 ± 0.8
PS50	50	59.9 ± 0.5	149.4 ± 0.9	39.1 ± 0.3	/	20.2 ± 0.2	21.6 ± 0.6
PS40	60	60.3 ± 0.4	149.0 ± 0.8	39.2 ± 0.2	/	18.4 ± 0.7	19.7 ± 0.2
PS30	70	62.5 ± 0.9	147.7 ± 0.6	39.7 ± 0.5	/	15.8 ± 0.3	16.9 ± 0.3
PS20	80	64.1 ± 0.8	147.3 ± 0.7	42.1 ± 0.4	/	13.5 ± 0.8	14.4 ± 0.1
PS10	90	65.3 ± 0.9	146.9 ± 0.8	42.5 ± 0.8	/	7.1 ± 0.4	7.6 ± 0.2
PS0	100	181.5 ± 0.3	/	42.7 ± 0.5	/	/	/

Fig. 3d is the first derivative of the curves in Fig. 3c, that shows the relationship between the decomposition rate of the sample and the changing temperature. During the initial heating phase (25–230 °C), the mass percent of the pure PLLA fibers (PS100) remained almost unchanged. However, with the addition of hydrophilic SF, there was greater mass loss as the higher amount of bound water present was heated off [84]. Figure S4b also shows the water loss of the composite material between 25 and 230 °C. The second stage of decomposition began at approximately 230 °C. For pure SF (PS0) and pure PLLA (PS100) nanofibers, the initial decomposition tem-

peratures (T_{onset}) were determined to be 294.31 °C and 341.84 °C respectively, which are consistent with literature reports [85–88]. The T_{onset} temperature of other composite fibers varied greatly from those of the pure SF and PLLA samples. This relationship showed that as the SF content increased, the T_{onset} temperature gradually decreased from 307.38 °C of the PS90 sample to 294.31 °C of the PS0 sample (Fig. 3c), but was always higher than that of pure silk fibroin. The maximum decomposition rate ranged from 32.95 %/min for the PS100 to 3.82 %/min for PS0 sample. This was most likely due to the breakdown of the molecular framework

and the decomposition of molecular domains present in the polymer blends [89]. As the temperature continued to rise to 450 °C, mainly carbon was retained [90]. So, as the silk content increased, more residue content was introduced. This finding is consistent with that of Wang et al. [78] as well. The study by Ghozali et al. [91] also reported that the thermal stability of polyethylene/poly-lactic acid composites is affected by the PLA content. Sheik et al. [90] cast silk and polyvinyl alcohol/polyvinylpyrrolidone (PVA/PVP) into a composite film, and found that the addition of silk could affect the maximum decomposition rate and the residual amount. In this study, under a nitrogen atmosphere, the addition of silk fibroin also slowed down the decomposition rate of the composite material at higher temperatures (450–550 °C). In conclusion, TG analysis proved the thermodynamic compatibility between the two different material phases, which was also supported by the DSC and morphological analysis [87].

3.4. Biological responses

An in vitro enzymatic degradation biodegradation study was then conducted in order to determine the materials biodegradability as it greatly influences a materials compatibility with living tissues [92]. The biodegradation rates of different PLLA/SF composites in an aqueous solution (Figure S5) and a protease solution (Fig. 4a) were compared to determine the enzymes effect on the composite materials. In the aqueous solution (Figure S5), it was observed that all samples exhibited very low degradation and their mass slowly decreased over the recorded period. SF could be easily decomposed by protease since the enzyme can easily cleave the protein chains. In the protease solution (Fig. 4a), the degree of degradation of pure silk fibroin nanofibers was much greater than the degradation rate of pure PLLA. This finding was also evident in the composite samples as the addition of silk fibroin promotes a much faster degradation rate. In addition, the morphology and structure of the fiber sample also greatly affected the degradation of the material. Samples with a higher porosity (PS90–PS60) were more like to degrade at a faster rate at the beginning (0–1 day) and then slowed down the degradation rate (1–6 days) as they had a large surface area for the degradation to take place first. While the samples with low porosity (PS50–PS10) tended to degrade evenly over time and obtained a similar final residual mass (~20%) on day 6. Samples treated with methanol for 30 min showed a similar trend like untreated samples under the enzymatic degradation (Figure S5b). However, the residual mass of each sample was greater after four

days. For the PS80 sample after 4 days, the residual mass increased from 50.2% of the untreated sample to 71.4% of the methanol-treated sample. This may be attributed to the increase of β -sheet crystals in silk fibroin after methanol treatment.

The hydrophilicity of biomaterials will affect the initial adhesion and migration of cells and the ability to tune this property can be very advantageous as certain cells favor a hydrophobic or hydrophilic material depending on the method of attachment [42]. The combination of hydrophilic silk fibroin and polylactic acid will help improve its hydrophilicity [93], as shown in Fig. 4b. The water contact angle of the pure SF fiber mat was 103°, and the water contact angle of the pure PLLA fiber mat was 135° and this showed the addition of more SF will gradually decrease the water contact angle on PS composite materials.

An in vitro cell study was then conducted to test the cellular compatibility and toxicity of PS composite nanofibers (Fig. 5, Figure S6). After staining with DAPI, it was found that the cells could successfully attach to all nanofiber samples when compared to the control group. The trend also indicated that cell viability increased as the porosity of PS samples increased or dominated SF proteins were added (Fig. 5b). After 48 h, the cells on PS composite nanomaterial still maintained favorable morphology, indicating that all ratios of PLLA and SF composite nanofibers supported the growth of mouse fibroblasts (L929) (Figure S6).

MTT test was used to evaluate the toxicity of nanofiber mats to L929 cells (Fig. 5b). When the samples were incubated with cells for 6 h, the difference in cell viability between different composite materials was not significant. After 24 h of incubation, all composite fibers had higher cell activity than pure PLLA fibers ($122.1 \pm 6.3\%$). Significantly, when the silk fibroin content was 10 wt% (sample PS90, $148.3 \pm 9.1\%$) and 20 wt% (sample PS80, $142.7 \pm 8.5\%$), the cell activity was greater than that of samples PS60 ($133.4 \pm 5.2\%$) and PS50 ($134.5 \pm 7.9\%$), (Fig. 5b). This phenomenon could also be observed from the photos under the fluorescence microscope (Fig. 5a). This was because PS90 and PS80 have smaller fiber diameter and higher total porosity compared to samples PS60 and PS50 as well as pure PLLA, thus providing more sites for cells growth. At the same time, the surface of a single fiber had a more nanopore structure, which was conducive to cell adhesion and differentiation [94,95] (Fig. 1). As the content of silk fibroin was differentiated, cell activity increased from $145.3 \pm 6.8\%$ of sample PS40 to $159.8 \pm 13.3\%$ of sample PS0, indicating that silk fibroin promotes cell growth better than PLLA synthetic polymer. After 48 h of cell proliferation, all results showed the same pattern as the result of 24 h culture.

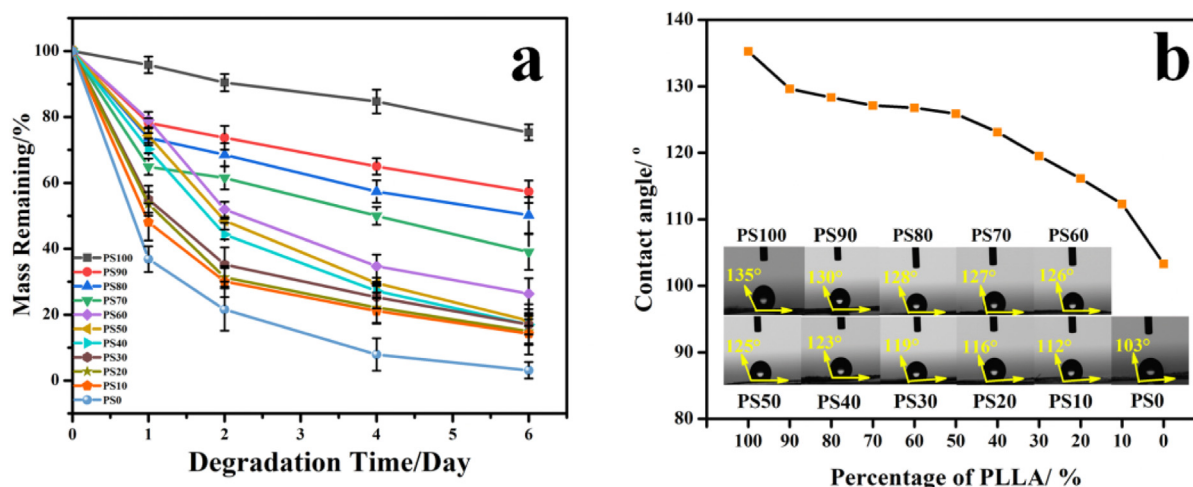


Fig. 4. In vitro biodegradation of PS composite nanofibers: the remaining mass of PS composite film was degraded in (a) a proteinase K solution for 1, 2, 4, and 6 days, respectively; (b) shows the water contact angle of PS composite nanofiber mats.

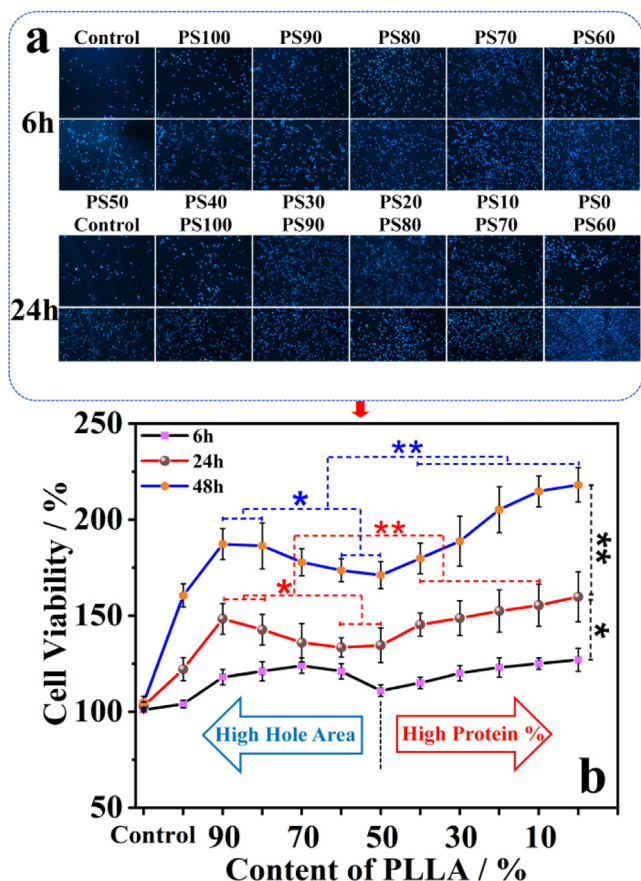


Fig. 5. (a) L929 cells attached to PS nanofiber materials were incubated for 6, 24 h (using DAPI staining and under fluorescence microscope); (b) The survival rates of mouse fibroblasts cultured on PS composite samples with different PLLA/silk fibroin mass ratios for 6, 24 and 48 h ($N \geq 3$, $p < 0.05$, $**p < 0.005$). An equivalent number of cells (1×10^4 /holes) on the orifice plate was used as the control.

However, in the result of 48 h cell culture, when the silk fibroin content was the main content, the cell activity increased significantly, and the cell activity of pure silk fibroin was higher than that of most composite samples. The proliferation and differentiation of cells in the long-term culture process suggested that the protein sequence provides better biological response to cell cultures

[96,97]. However, for PLLA dominated samples, the pores on the fiber surface had a more obvious effect on cell proliferation, both in the short-term and long-term cell culture studies.

3.5. Mechanism of nanofiber assembly

The combination of materials can overcome and improve the poor performance of single-phase materials, and fully take advantage of each separate material unique properties. Fig. 6 shows the molecular structures of pure PLLA (Fig. 6a), pure SF (Fig. 6A), the electrospinning composites (Fig. 6b, B) and their solvent volatilization process (Fig. 6c, d; C, D) to form the electrospun fibers (Fig. 6e, E). In this study, an environmentally-friendly low-boiling dichloromethane-formic acid solvent system was used to obtain a uniform PLLA/SF electrospinning solution. In the electrospinning process, the PLLA/SF solution first accumulated charges on the surface and formed a Taylor cone. When the electrostatic field force was greater than the surface tension, the PLLA and SF chains were stretched and aligned parallel to the fiber axis [98,99], promoted the formation of hydrogen bonds between C = O of PLLA and O-H of SF, which was verified by the structural analysis. As solution was being spun, it was drawn into fibers due to the electrostatic field, quickly volatilizes due to the heat in the environment. The jet in the electric field will undergo nanophase separation during its movement and there are two main reasons for the nanophase separation of the polymer solutions. The first was the change in the composition of the solution. For example, water vapor induces nanophase separation, and condensed water was used as a non-solvent. This type of nanophase separation caused by the deterioration of solvent solubility was called lyotropic phase separation. While the second reason was thermally induced nanophase separation. The polymer was dissolved in a solvent with a high boiling point and low volatility to form the homogeneous solution which was then cooled down and thermally induced nanophase separation.

In this study, the porous nanofibers were obtained through both these two reasons. When the PLLA content in the electrospinning solution was more than 50%, the surface heat of the jet was decreased during the solvent volatilization phase. Then the solvent's solubility worsens and part of the condensed water collects on the surface of the hydrophobic PLLA jet. The exchange of solvent and non-solvent (water) led to liquid-liquid phase separation to form two new phases: a polymer-rich phase and a polymer-poor

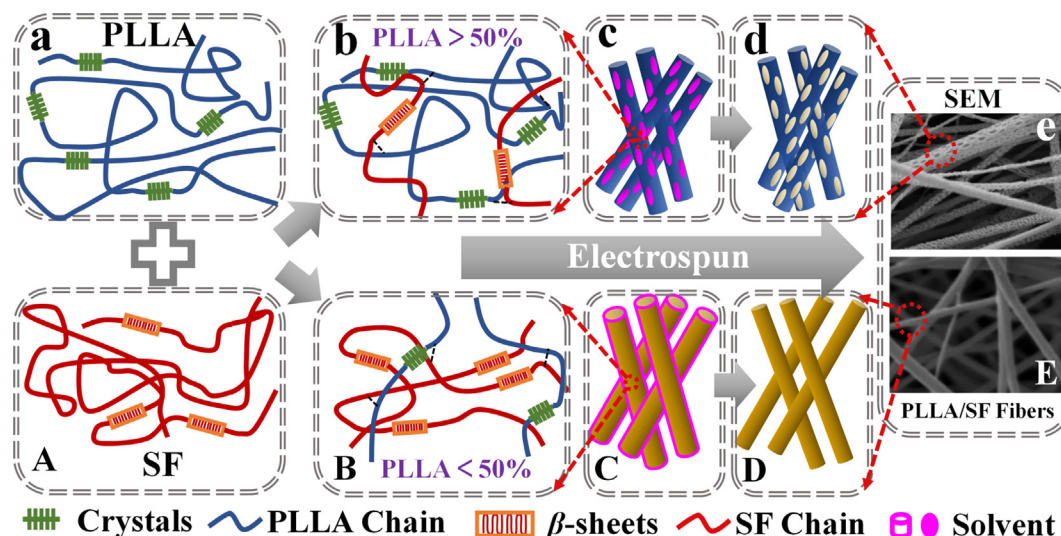


Fig. 6. The assembly mechanism of PS composite nanofiber materials with tunable pore structures.

phase [100]. When the polymer-rich phase was solidified, the solvent was removed to obtain a nanoporous structure [101]. With the increase of the hydrophilic silk fibroin content in the composite solution, the addition of silk fibroin increased the formic acid content in the solvent, which reduced the evaporation rate of the methylene chloride-formic acid solvent [102], resulting in a wide range of automatic phase separations that promoted the aggregation of more polymer-rich phases and solvent-rich phases. This in turn increased porosity and pore size of the nanofibers. This unique nanopore structure increased the specific surface area of the composite nanofibers, improved the hydrophilicity of the material and provided additional space for cell growth and proliferation [103]. When the PLLA content in the electrospinning solution was more than 50%, the electrospinning solution was dominated by silk fibroin proteins, the solvent could easily pass through the well-permeable SF/PLLA layer. At the same time, the solvent volatilizes away heat from the fiber surface and was released into the surrounding air. The condensed water attempts to adhere, but the hydrophilicity of silk fibroin prevents the condensed water from accumulating, and the solute-rich and solvent-rich areas were more difficult to form [102], so a swelling and smooth surface was formed on the fiber with a lower porosity [104]. The increase in protein content in the composite nanofiber mats also provided a favorable place for cell proliferation and differentiation [105].

In conclusion, by combining the electrospinning technology and the low boiling point solvent preparation method, a PLLA/SF composite nanofiber material with a controllable fiber surface structure had been successfully obtained. Although both pure PLLA and pure SF could be electrospun into a single fiber, it was difficult to meet the requirements of uniform diameter distribution alone. The addition of SF promoted the uniformity of electrospinning and enriched the functional structure of the fiber surface, and improved the biocompatibility and biodegradability of the material [105]. Therefore, this study had proven that the SF ratio could control the pore structure, size and uniformity on the fiber surface, which could produce highly efficient and biocompatible drug carriers or tissue scaffold materials that could greatly increase cell viability for biomedical applications.

4. Conclusion

In this study, a series of PLLA/SF nanoporous composite nanofibers were prepared by electrospun technology and demonstrated the ability to engineer the nanopore structure on a single nanofiber which is highly advantageous as it greatly increases the cell viability and attachment while creating a low toxicity environment for the cells to proliferate. The results of FTIR, XPS, XRD and DSC analysis showed that the gradual change of the composite material ratio can influence the structure of the resulting electrospun composite fibers. This was accomplished by changing β -sheet crystals content, the melting temperature, melting enthalpy and glass transition temperatures of the materials. Through detailed study on the thermal stability, hydrophilicity, in vitro degradability, and cell viability of the material, it was found that the composite materials retained favorable properties from both pure PLLA and SF and improved upon both separate materials. Water contact angle measurement and in vitro degradation experiments demonstrated that the silk fibroin content increased the hydrophilicity and the enzymatic degradation rate of the electrospun composites. This study provides a new platform for engineering proteins-synthetic polymer composite fibers on the nanoscale, and promotes the wide application of polylactic acid-based porous nanofibers in the biomedical field while also being highly environmentally friendly.

Declaration of Competing Interest

The authors declare that they have no known competing financial interests or personal relationships that could have appeared to influence the work reported in this paper.

Acknowledgements

This study is supported by the National Natural Science Foundation of China (21973045). K.P. and X.H. are supported by Rowan University Seed Research Grants, the US NSF Biomaterials Program (DMR-1809541) and Future Manufacturing Program (CMMI-2037097).

Appendix A. Supplementary material

Supplementary data to this article can be found online at <https://doi.org/10.1016/j.matdes.2022.111053>.

References

- [1] Y. Cui, Z. Wang, Z. Li, X. Ji, B. Yuan, Y. Sun, C. Peng, Y. Leng, M. Dou, J. Wang, H. Liu, Functionalized anti-osteoporosis drug delivery system enhances osseointegration of an inorganic-organic bioactive interface in osteoporotic microenvironment, *Mater. Des.* 206 (2021) 109753, <https://doi.org/10.1016/j.matdes.2021.109753>.
- [2] M. Gulfam, S. Jo, S.-W. Jo, T.T. Vu, S.H. Park, K.T. Lim, Highly porous and injectable hydrogels derived from cartilage cellularized matrix exhibit reduction and NIR light dual-responsive drug release properties for application in antitumor therapy, *NPG Asia Mater.* 14 (1) (2022) 1–17, <https://doi.org/10.1038/s41427-021-00354-4>.
- [3] A. Kourgiantaki, D.S. Tzeranis, K. Karali, K. Georgelou, E. Bampoula, S. Psilodimitrakopoulos, I.V. Yannas, E. Stratakis, K. Sidiropoulos, I. Charalampopoulos, A. Gravanis, Neural stem cell delivery via porous collagen scaffolds promotes neuronal differentiation and locomotion recovery in spinal cord injury, *npj Regen. Med.* 5 (1) (2020) 1–14, <https://doi.org/10.1038/s41536-020-0097-0>.
- [4] H. Samadian, S. Farzamfar, A. Vaez, A. Ehterami, A. Bit, M. Alam, A. Goodarzi, G. Darya, M. Salehi, A tailored polylactic acid/polycaprolactone biodegradable and bioactive 3D porous scaffold containing gelatin nanofibers and Taurine for bone regeneration, *Sci. Rep.* 10 (1) (2020) 1–12, <https://doi.org/10.1038/s41598-020-70155-2>.
- [5] M. Pasichnyk, J. Gašlová, P. Minarik, M. Václavíková, I. Melnyk, Development of polyester filters with polymer nanocomposite active layer for effective dye filtration, *Sci. Rep.* 12 (1) (2022) 1–12, <https://doi.org/10.1038/s41598-022-04829-4>.
- [6] P. Zhuang, X. Wu, H. Dai, Y. Yao, T. Qiu, Y. Han, S. Li, Nano β -tricalcium phosphate/hydrogel encapsulated scaffolds promote osteogenic differentiation of bone marrow stromal cells through ATP metabolism, *Mater. Des.* 208 (2021) 109881, <https://doi.org/10.1016/j.matdes.2021.109881>.
- [7] Z. Cui, J. Wu, J. Chen, X. Wang, J. Si, Q. Wang, Preparation of 3-D porous PVDF/TPU composite foam with superoleophilic/hydrophobicity for the efficient separation of oils and organics from water, *J. Mater. Sci.* 56 (21) (2021) 12506–12523, <https://doi.org/10.1007/s10853-021-05995-y>.
- [8] V.S. Seesala, R. Rajasekaran, A. Dutta, P.V. Vaidya, S. Dhara, Dense-porous multilayer ceramics by green shaping and salt leaching, *Open Ceramics* 5 (2021) 100084, <https://doi.org/10.1016/j.joceram.2021.100084>.
- [9] D. Hotza, M. Di Luccio, M. Wilhelm, Y. Iwamoto, S. Bernard, J.C. Diniz da Costa, Silicon carbide filters and porous membranes: A review of processing, properties, performance and application, *J. Membr. Sci.* 610 (2020) 118193, <https://doi.org/10.1016/j.memsci.2020.118193>.
- [10] Q. Cui, D.J. Bell, S.B. Rauer, M. Wessling, Wet-spinning of biocompatible core-shell polyelectrolyte complex fibers for tissue engineering, *Adv. Mater. Interfaces* 7 (23) (2020) 2000849, <https://doi.org/10.1002/admi.202000849>.
- [11] H. Liu, A. Ahlinder, M.A. Yassin, A. Finne-Wistrand, T. Gasser Christian, Computational and experimental characterization of 3D-printed PCL structures toward the design of soft biological tissue scaffolds, *Mater. Des.* 188 (2020), <https://doi.org/10.1016/j.matdes.2020.108488>.
- [12] T. Zhao, Y. Zheng, X. Zhang, D. Teng, Y. Xu, Y. Zeng, Design of helical groove/hollow nanofibers via tri-fluid electrospinning, *Mater. Des.* 205 (2021) 109705, <https://doi.org/10.1016/j.matdes.2021.109705>.
- [13] L. Shang, Y. Yu, Y. Liu, Z. Chen, T. Kong, Y. Zhao, Spinning and applications of bioinspired fiber systems, *ACS Nano* 13 (3) (2019) 2749–2772, <https://doi.org/10.1021/acsnano.8b09651>.
- [14] A. Ota, R. Beyer, U. Hageroth, A. Müller, P. Tomasic, F. Hermanutz, M.R. Buchmeiser, Chitin/cellulose blend fibers prepared by wet and dry-wet spinning, *Polym. Adv. Technol.* 32 (1) (2021) 335–342, <https://doi.org/10.1002/pat.5089>.

- [15] L. Wang, N.Z. Ezazi, L. Liu, R. Ajdary, W. Xiang, M. Borghei, H.A. Santos, O.J. Rojas, Microfibers synthesized by wet-spinning of chitin nanomaterials: mechanical, structural and cell proliferation properties, *RSC Adv.* 10 (49) (2020) 29450–29459, <https://doi.org/10.1039/D0RA06178F>.
- [16] L. Kubáč, O. Kodym, The impact of 3D printing technology on supply chain, MATEC web of conferences. EDP Sciences 134 (2017) 00027, <https://doi.org/10.1051/mateconf/201713400027>.
- [17] X. Wang, M. Jiang, Z. Zhou, J. Gou, D. Hui, 3D printing of polymer matrix composites: A review and prospective, *Compos. B Eng.* 110 (2017) 442–458, <https://doi.org/10.1016/j.compositesb.2016.11.034>.
- [18] X. Zhou, X.i. Cheng, D. Xing, Q.i. Ge, Y. Li, X. Luan, N. Gu, Y. Qian, Ca ions chelation, collagen I incorporation and 3D bionic PLGA/PCL electrospun architecture to enhance osteogenic differentiation, *Mater. Des.* 198 (2021) 109300, <https://doi.org/10.1016/j.matdes.2020.109300>.
- [19] J. Li, S. Wu, C. Wu, L. Qiu, G. Zhu, C. Cui, Y. Liu, W. Hou, Y. Wang, L. Zhang, I. Teng, H. Yang, W. Tan, Versatile surface engineering of porous nanomaterials with bioinspired polyphenol coatings for targeted and controlled drug delivery, *Nanoscale* 8 (16) (2016) 8600–8606, <https://doi.org/10.1039/C6NR00600K>.
- [20] W.F. Stanley, A.K. Bandaru, S. Rana, S. Parveen, S. Pichandi, Pichandi Subramani, Mechanical, dynamic-mechanical and wear performance of novel non-crimp glass fabric-reinforced liquid thermoplastic composites filled with cellulose microcrystals, *Mater. Des.* 212 (2021) 110276, <https://doi.org/10.1016/j.matdes.2021.110276>.
- [21] A. Amini, A. Khavari, F. Barthelat, A.J. Ehrlicher, Centrifugation and index matching yield a strong and transparent bioinspired nacreous composite, *Science* 373 (6560) (2021) 1229–1234, <https://doi.org/10.1126/science.abf0277>.
- [22] O. Adeniran, W. Cong, E. Bediako, S.P. Adu, Environmental affected mechanical performance of additively manufactured carbon fiber-reinforced plastic composites, *J. Compos. Mater.* 56 (7) (2022) 1139–1150, <https://doi.org/10.1177/00219983211066548>.
- [23] X. Dong, J. Zhang, L. Pang, J. Chen, M. Qi, S. You, N. Ren, An anisotropic three-dimensional electrospun micro/nanofibrous hybrid PLA/PCL scaffold, *RSC Adv.* 9 (17) (2019) 9838–9844, <https://doi.org/10.1039/C9RA00846B>.
- [24] Q. Deng, F. Wang, C.R. Gough, X. Hu, Tunable microphase-regulated silk fibroin/poly (lactic acid) biocomposite materials generated from ionic liquids, *Int. J. Biol. Macromol.* 197 (2022) 55–67, <https://doi.org/10.1016/j.ijbiomac.2021.12.060>.
- [25] J. Liu, T. Li, H. Zhang, W. Zhao, L. Qu, S. Chen, S. Wu, Electrospun strong, bioactive, and bioabsorbable silk fibroin/poly (L-lactic-acid) nanoyarns for constructing advanced nanotextile tissue scaffolds, *Materials Today Bio* 14 (2022) 100243, <https://doi.org/10.1016/j.mtbio.2022.100243>.
- [26] Y. Gao, W. Shao, W. Qian, J. He, Y. Zhou, K. Qi, L. Wang, S. Cui, R. Wang, Biomaterialized poly (l-lactic-co-glycolic acid)-tussah silk fibroin nanofiber fabric with hierarchical architecture as a scaffold for bone tissue engineering, *Mater. Sci. Eng., C* 84 (2018) 195–207, <https://doi.org/10.1016/j.msec.2017.11.047>.
- [27] C. Yan, Y. Ren, X. Sun, L. Jin, X. Liu, H. Chen, K. Wang, M. Yu, Y. Zhao, Photoluminescent functionalized carbon quantum dots loaded electroactive silk fibroin/PLA nanofibrous bioactive scaffolds for cardiac tissue engineering, *J. Photochem. Photobiol., B* 202 (2020) 111680, <https://doi.org/10.1016/j.jphotobiol.2019.111680>.
- [28] Y.K. Yeon, H.S. Park, J.M. Lee, J.S. Lee, Y.J. Lee, M.T. Sultan, Y.B. Seo, O.J. Lee, S.H. Kim, C.H. Park, New concept of 3D printed bone clip (polylactic acid/hydroxyapatite/silk composite) for internal fixation of bone fractures, *J. Biomater. Sci. Polym. Ed.* 29 (7–9) (2018) 894–906, <https://doi.org/10.1080/09205063.2017.1384199>.
- [29] K.H. Lee, H.F. Huang, C.T. Lo, Huang Hsui Feng, Lo Chieh Tsung, Influence of precursor solvent and confined environment on the polymorphic transition in electrospun Poly (l-lactide) fibers, *Polymer* 237 (2021) 124339, <https://doi.org/10.1016/j.polymer.2021.124339>.
- [30] C.M. Dadrás, A. Jalali-aran, U.J. Martínez, A comparison of the effect of silk fibroin nanoparticles and microfibers on the reprocessing and biodegradability of PLA/PCL blends, *J. Polym. Environ.* 29 (8) (2021) 2585–2597, <https://doi.org/10.1007/s10924-021-02053-1>.
- [31] Y. Deng, D. Zhang, N. Zhang, T. Huang, Y. Lei, Y. Wang, Electrospun stereocomplex polylactide porous fibers toward highly efficient oil/water separation, *J. Hazard. Mater.* 407 (2021), <https://doi.org/10.1016/j.jhazmat.2020.124787> 124787.
- [32] M. Dai, M. Li, J. Gong, L. Meng, B. Zhang, Y. Zhang, Y. Yin, J. Wang, Silk fibroin/gelatin/calcium alginate composite materials: Preparation, pore characteristics, comprehensive hemostasis in vitro, *Mater. Des.* 216 (2022) 110577, <https://doi.org/10.1016/j.matdes.2022.110577>.
- [33] X. Hu, D. Kaplan, P. Cebe, Determining beta-sheet crystallinity in fibrous proteins by thermal analysis and infrared spectroscopy, *Macromolecules* 39 (18) (2006) 6161–6170, <https://doi.org/10.1021/ma0610109>.
- [34] J. Kong, S. Yu, Fourier transform infrared spectroscopic analysis of protein secondary structures, *Acta biochimica et biophysica Sinica* 39 (8) (2007) 549–559, <https://doi.org/10.1111/j.1745-7270.2007.00320.x>.
- [35] Y. Zhao, B. Liu, C. You, M. Chen, Effects of MgO whiskers on mechanical properties and crystallization behavior of PLLA/MgO composites, *Mater. Des.* 89 (2016) 573–581, <https://doi.org/10.1016/j.matdes.2015.09.157>.
- [36] F. Yamin, F. Naddafun, S. Zohoori, Electrospinning of eucalyptus cellulose nano fiber and improving its properties by doping nano materials, *J. Nat. Fibers* (2021) 1–10, <https://doi.org/10.1080/15440478.2021.1932675>.
- [37] C.M. Srivastava, R. Purwar, A.P. Gupta, Enhanced potential of biomimetic, silver nanoparticles functionalized Antheraea mylitta (tasar) silk fibroin nanofibrous mats for skin tissue engineering, *Int. J. Biol. Macromol.* 130 (2019) 437–453, <https://doi.org/10.1016/j.ijbiomac.2018.12.255>.
- [38] Z. Wang, C. Zhao, Z. Pan, Porous bead-on-string poly (lactic acid) fibrous membranes for air filtration, *J. Colloid Interface Sci.* 441 (2015) 121–129, <https://doi.org/10.1016/j.jcis.2014.11.041>.
- [39] R. Casasola, N.L. Thomas, A. Trybala, S. Georgiadou, Electrospun poly lactic acid (PLA) fibres: Effect of different solvent systems on fibre morphology and diameter, *Polymer* 55 (18) (2014) 4728–4737, <https://doi.org/10.1016/j.polymer.2014.06.032>.
- [40] A. Opálková Šišková, K. Mosnáčková, J. Hruza, J. Frajová, A. Opálek, M. Bučková, K. Kozics, P. Peer, E. AndicsováAnita, Electrospun poly (ethylene terephthalate)/silk fibroin composite for filtration application, *Polymers* 13 (15) (2021) 2499, <https://doi.org/10.3390/polym13152499>.
- [41] O. Monticelli, S. Bocchini, L. Gardella, D. Cavallo, P. Cebe, G. Germelli, Impact of synthetic talc on PLLA electrospun fibers, *Eur. Polym. J.* 49 (9) (2013) 2572–2583, <https://doi.org/10.1016/j.eurpolymj.2013.05.017>.
- [42] J. Qin, Y. Jiang, J. Fu, Y. Wan, R. Yang, W. Gao, H. Wang, Evaluation of drug release property and blood compatibility of aspirin-loaded electrospun PLA/RSF composite nanofibers, *Iran. Polym. J.* 22 (10) (2013) 729–737, <https://doi.org/10.1007/s13726-013-0171-1>.
- [43] W. Shao, J. He, Q. Han, F. Sang, Q. Wang, L. Chen, S. Cui, B. Ding, A biomimetic multilayer nanofiber fabric fabricated by electrospinning and textile technology from polylactic acid and Tussah silk fibroin as a scaffold for bone tissue engineering, *Mater. Sci. Eng., C* 67 (2016) 599–610, <https://doi.org/10.1016/j.msec.2016.05.081>.
- [44] A. Aluigi, A. Varesano, C. Vineis, A. Del Rio, Electrospinning of immiscible systems: The wool keratin/polyamide-6 case study, *Mater. Des.* 127 (2017) 144–153, <https://doi.org/10.1016/j.matdes.2017.04.045>.
- [45] P. Cebe, B.P. Partlow, D.L. Kaplan, A. Wurm, E. Zhuravlev, C. Schick, Silk I and Silk II studied by fast scanning calorimetry, *Acta Biomater.* 55 (2017) 323–332, <https://doi.org/10.1016/j.actbio.2017.04.001>.
- [46] B. Cai, H. Gu, F. Wang, K. Printon, Z. Gu, X. Hu, Ultrasound regulated flexible protein materials: Fabrication, structure and physical-biological properties, *Ultrason. Sonochem.* 79 (2021) 105800, <https://doi.org/10.1016/j.ultrsonch.2021.105800>.
- [47] C. Sun, L. Zou, Y. Xu, Y. Wang, Ibuprofen-Loaded Poly (Lactic Acid) Electrospun Mats: The Morphology, Physicochemical Performance, and In Vitro Drug Release Behavior, *Macromol. Mater. Eng.* 305 (12) (2020) 2000457, <https://doi.org/10.1002/mame.202000457>.
- [48] S. Sheng, X. Hu, F. Wang, Q. Ma, M. Gu, Mechanical and thermal property characterization of poly-L-lactide (PLLA) scaffold developed using pressure-controllable green foaming technology, *Mater. Sci. Eng., C* 49 (2015) 612–622, <https://doi.org/10.1016/j.msec.2015.01.025>.
- [49] P. Taddei, S. Tozzi, G. Zuccheri, S. Martinotti, E. Ranzato, V. Chiono, I. Carmagnola, M. Tsukada, Intermolecular interactions between B. mori silk fibroin and poly(l-lactic acid) in electrospun composite nanofibrous scaffolds, *Mater. Sci. Eng., C* 70 (2017) 777–787, <https://doi.org/10.1016/j.msec.2016.09.055>.
- [50] Y. Hang, Y. Zhang, Y. Jin, H. Shao, X. Hu, Preparation of regenerated silk fibroin/silk sericin fibers by coaxial electrospinning, *Int. J. Biol. Macromol.* 51 (5) (2012) 980–986, <https://doi.org/10.1016/j.ijbiomac.2012.08.010>.
- [51] S. Hofmann, C.T. Wong Po Foo, F. Rossetti, M. Textor, G. Vunjak-Novakovic, D. L. Kaplan, H.P. Merkle, L. Meinel, Silk fibroin as an organic polymer for controlled drug delivery, *J. Control. Release* 111 (1–2) (2006) 219–227, <https://doi.org/10.1016/j.jconrel.2005.12.009>.
- [52] J. Zhong, M. Ma, W. Li, J. Zhou, Z. Yan, D. He, Self-assembly of regenerated silk fibroin from random coil nanostructures to antiparallel β -sheet nanostructures: Self-Assembly of Regenerated Silk Fibroin, *Biopolymers* 101 (12) (2014) 1181–1192, <https://doi.org/10.1002/bip.22532>.
- [53] M.A.d. Moraes, G.M. Nogueira, R.F. Weska, M.M. Beppu, Nogueira Grinia Michelle, Weska Raquel Farias, BeppuMarisa Masumi, Preparation and characterization of insoluble silk fibroin/chitosan blend films, *Polymers* 2 (4) (2010) 719–727, <https://doi.org/10.3390/polym2040719>.
- [54] J. Halim, K.M. Cook, M. Naguib, P. Eklund, Y. Gogotsi, J. Rosen, M.W. Barsoum, X-ray photoelectron spectroscopy of select multi-layered transition metal carbides (MXenes), *Appl. Surf. Sci.* 362 (2016) 406–417, <https://doi.org/10.1016/j.apsusc.2015.11.089>.
- [55] D. Badillo-Sanchez, D. Chelazzi, R. Giorgi, A. Cincinelli, P. Baglioni, Understanding the structural degradation of South American historical silk: A Focal Plane Array (FPA) FTIR and multivariate analysis, *Sci. Rep.* 9 (1) (2019) 1–10, <https://doi.org/10.1038/s41598-019-53763-5>.
- [56] J. Hou, G. Zhou, J. Hu, Y. Wang, S. Gao, Preparation and evaluation of PLA/PVP core-shell microparticles mat via single capillary electrospinning as a potential drug-loading material, *Polym. Bull.* 79 (4) (2022) 2173–2188, <https://doi.org/10.1007/s00289-021-03613-0>.
- [57] S. Bagus Paul, S. Ilton Eugene, C.J. Nelin, The interpretation of XPS spectra: Insights into materials properties, *Surf. Sci. Rep.* 68 (2) (2013) 273–304, <https://doi.org/10.1016/j.surfrep.2013.03.001>.
- [58] Y. Zhang, Y. Su, J. Peng, X. Zhao, J. Liu, J. Zhao, Z. Jiang, Composite nanofiltration membranes prepared by interfacial polymerization with natural material tannic acid and trimethylol chloride, *J. Membr. Sci.* 429 (2013) 235–242, <https://doi.org/10.1016/j.memsci.2012.11.059>.
- [59] K. Boonpavanitchakul, S. Jarussophon, N. Pimpha, W. Kangwansupamonkon, R. Magaraphan, Silk sericin as a bio-initiator for grafting from synthesis of

- poly(lactide) via ring-opening polymerization, *Eur. Polym. J.* 121 (2019), <https://doi.org/10.1016/j.eurpolymj.2019.109265> 109265.
- [60] N. Ojah, D. Saikia, D. Gogoi, P. Baishya, G.A. Ahmed, A. Ramteke, A.J. Choudhury, Surface modification of core-shell silk/PVA nanofibers by oxygen dielectric barrier discharge plasma: Studies of physico-chemical properties and drug release behavior, *Appl. Surf. Sci.* 475 (2019) 219–229, <https://doi.org/10.1016/j.apsusc.2018.12.270>.
- [61] D. Li, W. Frey Margaret, D. Vynias, J. Baumner Antje, Availability of biotin incorporated in electrospun PLA fibers for streptavidin binding, *Polymer* 48 (21) (2007) 6340–6347, <https://doi.org/10.1016/j.polymer.2007.08.027>.
- [62] K. Hodak Satreerat, T. Supasai, B. Paosawatyanong, K. Kamlangkla, V. Pavarajarn, Enhancement of the hydrophobicity of silk fabrics by SF6 plasma, *Appl. Surf. Sci.* 254 (15) (2008) 4744–4749, <https://doi.org/10.1016/j.apsusc.2008.01.110>.
- [63] J. Shao, C. Chen, Y. Wang, X. Chen, C. Du, Early stage structural evolution of PLLA porous scaffolds in thermally induced phase separation process and the corresponding biodegradability and biological property, *Polym. Degrad. Stabil.* 97 (6) (2012) 955–963, <https://doi.org/10.1016/j.polymerdegradstab.2012.03.014>.
- [64] S. Chen, S. Liu, L. Zhang, Q. Han, H. Liu, J. Shen, G. Li, L. Zhang, Y. Yang, Construction of injectable silk fibroin/polydopamine hydrogel for treatment of spinal cord injury, *Chem. Eng. J.* 399 (2020), <https://doi.org/10.1016/j.cej.2020.125795> 125795.
- [65] J. Wang, B. Sun, M.A. Bhatto, T. Zhu, K. Yu, J. Bao, Y. Morsi, H. El-Hamshary, M. El-Newehy, X. Mo, Fabrication and characterization of *Antheraea pernyi* silk fibroin-blended P(LLA-CL) nanofibrous scaffolds for peripheral nerve tissue engineering, *Front. Mater. Sci.* 11 (1) (2017) 22–32, <https://doi.org/10.1007/s11706-017-0368-x>.
- [66] Z. Zhong, Q. Guo, Y. Mi, Solid-state nmr investigation of crosslinkable blends of novolac and poly (ϵ -caprolactone), *Polymer* 40 (1) (1999) 27–33, [https://doi.org/10.1016/S0032-3861\(98\)00242-0](https://doi.org/10.1016/S0032-3861(98)00242-0).
- [67] K. Suganuma, H. Matsuda, T. Asakura, Characterization of polyurethane and a silk fibroin-polyurethane composite fiber studied with NMR spectroscopies, *Polym. J.* 54 (6) (2022) 803–813, <https://doi.org/10.1038/s41428-022-00629-9>.
- [68] Y. Nakazawa, T. Asakura, High-Resolution 13C CP/MAS NMR Study on Structure and Structural Transition of *Antheraea pernyi* Silk Fibroin Containing Poly (L-alanine) and Gly-Rich Regions, *Macromolecules* 35 (6) (2002) 2393–2400, <https://doi.org/10.1021/ma011999t>.
- [69] C. Wu, Poly(lactide)-based renewable composites from natural products residues by encapsulated film bag: characterization and biodegradability, *Carbohydr. Polym.* 90 (1) (2012) 583–591, <https://doi.org/10.1016/j.carbpol.2012.05.081>.
- [70] K.-H. Zhang, Q.-Z. Yu, X.-M. Mo, Fabrication and intermolecular interactions of silk fibroin/hydroxybutyl chitosan blended nanofibers, *Int. J. Mol. Sci.* 12 (4) (2011) 2187–2199, <https://doi.org/10.3390/ijms12042187>.
- [71] Q. Ma, M. Pyda, B. Mao, P. Cebe, Relationship between the rigid amorphous phase and mesophase in electrospun fibers, *Polymer* 54 (10) (2013) 2544–2554, <https://doi.org/10.1016/j.polymer.2013.03.019>.
- [72] H. Chen, M. Pyda, P. Cebe, Non-isothermal crystallization of PET/PLA blends, *Thermochim. Acta* 492 (1–2) (2009) 61–66, <https://doi.org/10.1016/j.tca.2009.04.023>.
- [73] A. Yadav, A. Kumar, K. Singh Pradeep, K. Sharma, Glass transition temperature of functionalized graphene epoxy composites using molecular dynamics simulation, *Integr. Ferroelectr.* 186 (1) (2018) 106–114, <https://doi.org/10.1080/10584587.2017.1370331>.
- [74] F. Wang, H. Liu, Y. Li, Q. Ma, J. Zhang, X. Hu, Tunable Biodegradable Poly(lactide)-Silk Fibroin Scaffolds Fabricated by a Solvent-Free Pressure-Controllable Foaming Technology, *ACS Applied Bio Materials* 3 (12) (2020) 8795–8807, <https://doi.org/10.1021/acsabm.0c01157>.
- [75] V.R. Timergaliev, C.G.M. Gennari, F. Cilirzo, R.I. Moustafine, Moustafine Rouslan I. Interpolyelectrolyte complexes based on Carbopol and oppositely charged polymer as new carriers for oral controlled diclofenac delivery, *Polym. Adv. Technol.* 32 (7) (2021) 2744–2752, <https://doi.org/10.1002/pat.5256>.
- [76] X. Hu, P. Cebe, A.S. Weiss, F. Omenetto, D.L. Kaplan, Protein-based composite materials, *Mater. Today* 15 (5) (2012) 208–215, [https://doi.org/10.1016/S1369-7021\(12\)7009-3](https://doi.org/10.1016/S1369-7021(12)7009-3).
- [77] F. Wang, N. Wolf, E.M. Rocks, T. Vuong, X. Hu, Comparative studies of regenerated water-based Mori, Thai, Eri, Muga and Tussah silk fibroin films, *J. Therm. Anal. Calorim.* 122 (3) (2015) 1069–1076, <https://doi.org/10.1007/s10973-015-4736-4>.
- [78] F. Wang, P. Chandler, R. Oszust, E. Sowell, Z. Graham, W. Ardito, X. Hu, Thermal and structural analysis of silk-poly(vinyl acetate) blends, *J. Therm. Anal. Calorimetr* 127 (1) (2017) 923–929, <https://doi.org/10.1007/s10973-016-5774-2>.
- [79] C.M. Srivastava, R. Purwar, R. Kannaujia, D. Sharma, Flexible silk fibroin films for wound dressing, *Fibers Polym.* 16 (5) (2015) 1020–1030, <https://doi.org/10.1007/s12221-015-1020-y>.
- [80] R. Androsch, K. Jariyavidyanont, C. Schick, Enthalpy relaxation of polyamide 11 of different morphology far below the glass transition temperature, *Entropy* 21 (10) (2019) 984, <https://doi.org/10.3390/e21100984>.
- [81] I. Weitzhandler, M. Dzuricky, I. Hoffmann, F. Garcia Quiroz, M. Gradzielski, A. Chilkoti, Micellar Self-Assembly of Recombinant Resilin-/Elastin-Like Block Copolypeptides, *Biomacromolecules* 18 (8) (2017) 2419–2426, <https://doi.org/10.1021/acs.biomac.7b00589>.
- [82] H. Yin, Y.Z. Chua, B. Yang, C. Schick, W.J. Harrison, P.M. Budd, M. Böhning, A. Schönhals, First Clear-Cut Experimental Evidence of a Glass Transition in a Polymer with Intrinsic Microporosity: PIM-1, *J. Phys. Chem. Lett.* 9 (8) (2018) 2003–2008, <https://doi.org/10.1021/acs.jpclett.8b00422>.
- [83] A. Ledeti, T. Olariu, A. Caunii, G. Vlase, D. Circioban, B. Baul, I. Ledeti, T. Vlase, M. Murariu, Evaluation of thermal stability and kinetic of degradation for levodopa in non-isothermal conditions, *J. Therm. Anal. Calorim.* 131 (2) (2018) 1881–1888, <https://doi.org/10.1007/s10973-017-6671-z>.
- [84] S.S. Shera, R.M. Banik, Development of Tunable Silk Fibroin/Xanthan Biopolymeric Scaffold for Skin Tissue Engineering Using L929 Fibroblast Cells, *J. Bionic Eng.* 18 (1) (2021) 103–117, <https://doi.org/10.1007/s42235-021-0004-4>.
- [85] F. Wang, H. Wu, V. Venkataraman, X. Hu, Silk fibroin-poly (lactic acid) biocomposites: Effect of protein-synthetic polymer interactions and miscibility on material properties and biological responses, *Mater. Sci. Eng., C* 104 (2019) 109890, <https://doi.org/10.1016/j.msec.2019.109890>.
- [86] K. Luo, Z. Shao, A novel regenerated silk fibroin-based hydrogels with magnetic and catalytic activities, *Chin. J. Polym. Sci.* 35 (4) (2017) 515–523, <https://doi.org/10.1007/s10118-017-1910-0>.
- [87] N.M. Bexiga, A.C. Bloise, M.A. de Moraes, A. Converti, M.M. Beppu, B. Polakiewicz, Production and characterization of fibroin hydrogel using waste silk fibers, *Fibers Polym* 18 (1) (2017) 57–63, <https://doi.org/10.1007/s12221-017-6805-8>.
- [88] S. Xiang, L. Feng, X. Bian, G. Li, X. Chen, Evaluation of PLA content in PLA/PBAT blends using TGA, *Polym. Test.* 81 (2020), <https://doi.org/10.1016/j.polymertesting.2019.106211> 106211.
- [89] X. Feng, J. Chen, J. Zhang, Y. Guo, Structure and Property Characteristics of Nano-TiO₂ Modified Silk Fibroin Composite Films Prepared with Sol-Gel Method, *Acta Chim. Sinica* 64 (22) (2006) 2281–2286, <https://doi.org/10.1021/ja0657206>.
- [90] S. Sheik, G.K. Nagaraja, K. Prashantha, Effect of silk fiber on the structural, thermal, and mechanical properties of PVA/PVP composite films, *Polym. Eng. Sci.* 58 (11) (2018) 1923–1930, <https://doi.org/10.1002/pen.24801>.
- [91] M. Ghozali, B. Sinaga Pius Doni, S. Maranata, Rohmah Elfi Nur. Study and Development of Linier Low Density Polyethylene (LLDPE) and Poly Lactic Acid (PLA) Biodegradable Compounds Using Compatibilizer LLDPE-g-MA, *World, Chem. Eng. J.* 1 (2) (2016) 11–16, <https://doi.org/10.36055/wcej.v1i2.802>.
- [92] L. Yu, Y.u. Chen, M. Wu, X. Cai, H. Yao, L. Zhang, H. Chen, J. Shi, “Manganese extraction” strategy enables tumor-sensitive biodegradability and theranostics of nanoparticles, *J. Am. Chem. Soc.* 138 (31) (2016) 9881–9894, <https://doi.org/10.1021/jacs.6b04299>.
- [93] L. Tian, M.P. Prabhakaran, J. Hu, M. Chen, F. Besenbacher, S. Ramakrishna, Coaxial electrospun poly (lactic acid)/silk fibroin nanofibers incorporated with nerve growth factor support the differentiation of neuronal stem cells, *RSC Adv.* 5 (62) (2015) 49838–49848, <https://doi.org/10.1039/C5RA05773F>.
- [94] B. Chang, W. Song, T. Han, J. Yan, F. Li, L. Zhao, H. Kou, Y. Zhang, Influence of pore size of porous titanium fabricated by vacuum diffusion bonding of titanium meshes on cell penetration and bone ingrowth, *Acta Biomater.* 33 (2016) 311–321, <https://doi.org/10.1016/j.actbio.2016.01.022>.
- [95] Y. Tian, H. Zheng, G. Zheng, P. Hu, Y. Li, Y. Lin, Q. Gao, X. Yao, R. Gao, C. Li, X. Wu, L. Sui, Hierarchical microgroove/nanopore topography regulated cell adhesion to enhance osseointegration around intrasosseous implants in vivo, *Biomater. Sci.* 10 (2) (2022) 560–580, <https://doi.org/10.1039/D1BM01657A>.
- [96] S. Rother, V.D. Galiazzi, D. Kilian, K.M. Fiebig, J. Becher, S. Moeller, U. Hempel, M. Schnabelrauch, J. Waltenberger, D. Scharnweber, V. Hintze, Hyaluronan/Collagen Hydrogels with Sulfated Hyaluronan for Improved Repair of Vascularized Tissue Tune the Binding of Proteins and Promote Endothelial Cell Growth, *Macromol. Biosci.* 17 (11) (2017) 1700154, <https://doi.org/10.1002/mabi.201700154>.
- [97] G. Song, C. Zheng, Y. Liu, M. Ding, P. Liu, J. Xu, W. Wang, J. Wang, In vitro extracellular matrix deposition by vascular smooth muscle cells grown in fibroin scaffolds, and the regulation of TGF- β 1, *Mater. Des.* 199 (2021) 1070154, <https://doi.org/10.1016/j.matdes.2020.109428>.
- [98] Q. Xie, X. Chang, Q. Qian, P. Pan, C.Y. Li, Structure and Morphology of Poly (lactic acid) Stereocomplex Nanofiber Shish Kebabs, *ACS Macro Lett.* 9 (1) (2020) 103–107, <https://doi.org/10.1021/acsmacrolett.9b00953>.
- [99] X. Meng, X. Wang, B. Zhang, Y. Zhang, Y. Jiang, M. Guo, Q. Li, Fibrous scaffold with a tunable nonlinear elasticity, *Polym. Test.* 94 (2021), <https://doi.org/10.1016/j.polymertesting.2020.107045> 107045.
- [100] Y. Wang, H. Huang, G. Li, X. Zhao, L. Yu, C. Zou, Y. Xu, Electrospun TiO₂-SiO₂ fibres with hierarchical pores from phase separation, *CrystEngComm* 19 (19) (2017) 2673–2680, <https://doi.org/10.1039/C7CE00471K>.
- [101] C. Önder Özgün, E. Yilgör, I. Yilgör, Fabrication of rigid poly (lactic acid) foams via thermally induced phase separation, *Polymer* 107 (2016) 240–248, <https://doi.org/10.1016/j.polymer.2016.11.025>.
- [102] Y. Sun, J. Liu, Y. Ding, Y. Han, Controlling the surface composition of PCBM in P3HT/PCBM blend films by using mixed solvents with different evaporation rates, *Chin. J. Polym. Sci.* 31 (7) (2013) 1029–1037, <https://doi.org/10.1007/s10118-013-1295-7>.
- [103] A. Gao, Q. Yang, L. Xue, Poly (L-Lactic acid)/silk fibroin composite membranes with improved crystallinity and thermal stability from non-solvent induced phase separation processes involving hexafluoroisopropanol, *Compos. Sci. Technol.* 132 (2016) 38–46, <https://doi.org/10.1016/j.compscitech.2016.06.011>.

- [104] L. Heichel Danielle, H. Vy Ngoc Chau, P. Ward Shawn, H. Adamson Douglas, K. A. Burke, Controlled radical polymerization of hydrophilic and zwitterionic brush-like polymers from silk fibroin surfaces, *J. Mater. Chem. B* 8 (45) (2020) 10392–10406, <https://doi.org/10.1039/D0TB01990A>.
- [105] P. Ivanchenko, J.M. Delgado-López, M. Iafisco, J. Gómez-Morales, A. Tampieri, G. Martra, Y. Sakhno, On the surface effects of citrates on nano-apatites: evidence of a decreased hydrophilicity, *Sci. Rep.* 7 (1) (2017) 1–10, <https://doi.org/10.1038/s41598-017-09376-x>.